

ASSESSING THE INTEGRATION AND PRE-PROCESSING OF NEON AIRBORNE
REMOTE SENSING AND IN-SITU DATA FOR OPTIMAL TREE SPECIES
CLASSIFICATION

by

VICTORIA MARY SCHOLL

B.S., Rochester Institute of Technology, 2016

A thesis submitted to the
Faculty of the Graduate School of the
University of Colorado in partial fulfillment
Of the requirement for the degree of
Master of Arts
Department of Geography

2019

This thesis entitled:
Assessing the integration and pre-processing of NEON airborne remote sensing and in-situ data
for optimal tree species classification
written by Victoria Mary Scholl
has been approved for the Department of Geography

Jennifer K. Balch

Colleen E. Reid

Date April 10, 2019

The final copy of this thesis has been examined by the signatories, and we
find that both the content and the form meet acceptable presentation standards
of scholarly work in the above mentioned discipline.

Scholl, Victoria Mary (M.A., Geography)

Assessing the integration and pre-processing of NEON airborne remote sensing and in-situ data
for optimal tree species classification

Thesis directed by Associate Professor Jennifer K. Balch

Accurately mapping tree species composition and diversity is a critical step towards understanding how forests recover in response to disturbances. The National Ecological Observatory Network (NEON) is a valuable source of open ecological data for sites across the United States. Freely available NEON data include *in-situ* measurements of individual tree species, stem locations, and crown diameter, along with hyperspectral, multispectral, and LiDAR airborne remote sensing image products. By linking these field-based and airborne NEON data, this study explores the impact of different types of training data preparation and preprocessing on coniferous tree species classification at the Niwot Ridge Mountain Research Station (NIWO) subalpine forest NEON site in Colorado. Pixel-based random forest (RF) machine learning models were trained using a series of reference data sets along with remote sensing raster data as descriptive features. The highest classification accuracies, 73% and 68% based on internal OOB error and an independent validation set, respectively, were achieved using all polygons created with half the maximum crown diameter per tree. The LiDAR-derived data products were found to be the most important remote sensing data-derived features, generally followed by vegetation indices. Incorporating LiDAR point cloud metrics, refining the reference data alignment with the remote sensing imagery, and transferring this pixel-based analysis to object-based classification using individual tree crowns are all promising directions for future analyses. This work contributes to the open development of well-labeled training data sets and reproducible forest composition mapping efforts.

ACKNOWLEDGEMENTS

I am grateful to the CU Boulder Earth Lab faculty, staff, and students who provided valuable advice and feedback on the design and execution of this study. The National Ecological Observatory Network is a program sponsored by the National Science Foundation and operated under cooperative agreement by Battelle Memorial Institute. This material is based in part upon work supported by the National Science Foundation through the NEON Program.

CONTENTS

CHAPTER

1. INTRODUCTION.....	1
2. BACKGROUND.....	5
3. METHODS.....	15
4. RESULTS.....	27
5. DISCUSSION.....	35
6. CONCLUSIONS.....	41
REFERENCES.....	42
APPENDIX.....	47
A. SPECTRAL REFLECTANCE CURVES EXTRACTED PER SPECIES.....	47
B. SPECTRAL REFLECTANCE CURVES OVERLAID.....	50
C. INTERSPECIES COMPARISON OF VARIABLES.....	53
D. VARIABLE IMPORTANCE.....	56

TABLES

Table

1. Tree species information.....	16
2. NEON data product descriptions.....	17
3. Remote sensing-derived feature descriptions.....	24
4. Number of trees and pixels per reference set.....	26
5. Overall accuracies for species classification.....	32
6. Overall accuracies when sample size is reduced.....	33
7. Confusion matrices.....	34

FIGURES

Figure

1. Remote sensing data spatial resolution comparison.....	9
2. Study Area.....	15
3. Reference set using all available <i>in-situ</i> data.....	18
4. Reference set using neon_veg workflow.....	21
5. Mean spectral reflectance per species.....	28
6. Mean spectral reflectance for all species overlaid.....	29
7. Interspecies variable comparison.....	30
8. Variable importance ranking.....	31

CHAPTER 1

INTRODUCTION

The world's forests are complex systems that are essential to many global processes (Bonan et al., 2008; Watson et al., 2018). Forests are experiencing unprecedented changes due to ongoing climate change and other types of natural and anthropogenic disturbances, including wildfire (Westerling et al. 2006), insect outbreaks (Bentz et al. 2010), and drought (Greenwood et al., 2017). Disturbances are events that alter forest patterns and processes, and they may interact in surprising and important ways (Pickett and White, 1985; Turner 2005; Buma 2015). Compound disturbances occur simultaneously or sequentially, producing an unpredictable effect that is different from the sum of the separate disturbances (Paine et al. 1998). Linked disturbances may amplify or dampen the extent, severity, or probability of subsequent disturbance occurrence (Simard et al., 2011). After being disturbed, forests may show signs of resilience and return to their pre-disturbance structure and function (Holling 1973), or they may shift to an alternative state of being (Scheffer et al. 2001). We have not yet quantified regional rates of forest recovery and resilience in response to large interacting disturbances, which are anticipated to increase in the future (Seidl et al., 2017). Key limitations to our understanding and modeling of post-disturbance resilience are a lack of data describing forest composition and diversity at the individual tree level.

The advent of remote sensing allows us to more efficiently estimate biophysical parameters of trees across large forested areas over time (Coops et al., 2004). Airplanes offer valuable spatial and temporal flexibility for data collection and are commonly used to map vegetation at local to regional scales. Many studies highlight the benefits of fusing diverse types

of airborne multispectral, hyperspectral, and light detection and ranging (LiDAR) data for optimal extraction of vegetation properties from remote sensing data (Dalponte et al. 2008, Asner et al., 2012; Stavros et al., 2017; Liu et al. 2017). In addition to estimating land cover and functional types across forested areas (Hansen et al. 2013; Asner et al., 2017), these spectral and structural data are shown to be useful predictors for estimating tree species and biophysical metrics such as biomass for both pixels and object-based image analysis using various classification techniques (Kaartinen et al., 2012; Fassnacht et al., 2016).

Large amounts of open ecological and remote sensing data are becoming increasingly available in recent years (Michener, 2015; Fassnacht et al., 2016). A notable source of these data is the National Ecological Observatory Network (NEON), a National Science Foundation (NSF) funded Grand Challenge project, awarded with the purpose of measuring ecological change for a span of 30 years (Keller et al., 2008). With its free, publicly available field-based and airborne remote sensing data products, NEON provides a valuable opportunity to study forest dynamics across the western United States. The NEON Airborne Observation Platform (AOP) collects multispectral, hyperspectral, and LiDAR imagery at sites across the United States and generates publicly available image data products with high spatial resolutions, ranging from 0.1 to 1 meters. Field-based measurements, including stem location, maximum crown diameter, and species of individual trees within selected sampling plots are collected, following standardized protocols every 1 to 3 years, in synchrony with AOP flights, when possible (Kampe et al., 2010). Species-level identification can theoretically be performed by linking these remote sensing and in-situ data, although the alignment of field-based data with remote sensing observations is a critical, yet challenging, aspect of these efforts (Graves et al., 2018). Open competitions in which many groups work to solve a problem using a common data set often lead to noteworthy

methodological advances (Carpenter, 2011). A recent ecological data science competition has tasked research groups with tree crown segmentation, alignment of data, and species classification at the open canopy longleaf pine ecosystem at the Ordway-Swisher Biological Station in Florida (Marconi et al., 2019). This explosion of collaborative open data exploration and processing methods for tree species classification is encouraging, although the highly diverse flora across NEON sites requires further assessment of methods based on local vegetation characteristics.

This study integrates NEON *in-situ* tree measurements with AOP remote sensing data at the closed canopy subalpine forest site at the Niwot Ridge Mountain Research Station (NIWO) within the Southern Rockies domain, where large interacting disturbances are prevalent. The impact of various types of training data preparation and preprocessing on pixel-based classification accuracy of the four dominant conifer species was investigated using the random forest (RF) machine learning technique. Training sets were created for tree stem point locations, circular polygons based on the maximum crown diameter of each individual tree, and also circular polygons with half of the maximum crown diameter of each individual as an intermediate size. An open R code workflow is proposed to filter short, suppressed trees and clip overlapping crowns to allow the taller trees to take precedence in layered canopies. Variable importance was used to assess the contribution of each remote sensing data product to the species classification. It was expected that the filtering and clipping steps would improve species classification, when compared to utilizing all available field-based observations to train the RF classifier. It was also expected that the half-diameter polygons would yield the best species classification accuracies, because they capture more variation in signal than individual stem points do, but are less likely to contain mixed pixels, as larger polygons would capture. This

work provides an initial species classification assessment at the NIWO site in Colorado and contributes to the open development of well-labeled training data sets and forest composition mapping efforts.

CHAPTER 2

BACKGROUND

2.1 National ecological observatory network (NEON)

The National Ecological Observatory Network (NEON) (<https://www.neonscience.org/>) is a National Science Foundation (NSF) funded Grand Challenge project, awarded with the purpose of measuring ecological change for a span of 30 years (Kampe et al., 2010). 81 NEON field sites are strategically distributed across the United States, within 20 distinct eco-climatic domains. The study area of this research is the Niwot Ridge (NIWO) site located in Domain 13, Southern Rockies and Colorado Plateau. NEON sampling efforts include in-situ individual plant measurements and airborne remote sensing.

2.2 NEON airborne remote sensing

NEON's sampling suite includes the Airborne Observation Platform (AOP), which carries a suite of three remote sensing instruments: multispectral (RGB) digital camera, NEON imaging spectrometer (NIS), and small-footprint LiDAR. Coincident capture of these three data sets is powerful and practical for high spatial resolution ecosystem monitoring. Spectral and structural properties of vegetation are closely tied to plants' biochemical composition and health (Kampe et al., 2010). Fusing multispectral, hyperspectral, and LiDAR data has been shown to improve derived forest metrics compared to using any of the methods alone (Anderson et al., 2008; Dalponte et al., 2008; Asner et al., 2012). The NEON project has established observation sites across the continental U.S. to monitor climate change, land use change, and invasive species. The forests within the terrestrial sites are representative of the diverse ecosystems and

climates present throughout the United States. During its annual flight campaign, the AOP flies over core NEON sites throughout the country at 90% of maximum greenness or greater, typically at an altitude of 1000 meters above ground level, and generates publicly available remote sensing data (Schimel and Keller, 2015). The data products are available as both flightlines and 1 km by 1 km mosaic tiles. The mosaic tiles have corners spatially referenced to an even kilometer and are projected into the Universal Transverse Mercator (UTM) mapping frame. When multiple flight lines cover a given tile, the most-nadir pixels are selected for the final mosaic. The AOP instruments and their relevant data products utilized in this study are described in further detail below.

2.2.1 Imaging spectrometer

The NEON Imaging Spectrometer (NIS) is a pushbroom collection-style instrument that measures reflected light energy with 426 narrow spectral bands, spanning the visible (380 nm) to shortwave infrared (2510 nm) wavelengths, with a spectral sampling of 5 nm. NEON implements calibration and atmospheric corrections to convert at-sensor radiance to surface reflectance [NEON.DOC.001288]. Raster data products generated from this hyperspectral reflectance include “Spectrometer orthorectified surface directional reflectance - mosaic” and “Vegetation Indices”, each with a spatial resolution of 1 meter. The surface reflectance data for all 426 spectral bands is available as an open HDF5 format. The Vegetation Indices are a collection of seven spectral indices that are known to be indicators of vegetation health: ARVI, EVI, NDLI, NDNI, NDVI, PRI, SAVI [described in NEON.DOC.002391]. These vegetation indices are calculated using well-known equations from scientific literature, using NIS surface

reflectance data as the input. The Vegetation Indices data product is distributed in the GeoTIFF format, in which each band contains a different vegetation index.

2.2.2 LiDAR

NEON operates two Optech ALTM Gemini systems and a Riegl LMS-Q780, used to collect discrete and waveform light detection and ranging (LiDAR) data at a spatial resolution of approximately 1-4 points/waveforms per square meter. These LiDAR instruments operate at a laser wavelength of 1064 nm in order to describe vegetation cover, height, shape, and vertical structure and underlying terrain. The discrete return LiDAR point cloud data is available from NEON, but for this exploratory study only the readily available raster data products (derived from the point cloud and distributed by NEON as 1km by 1km tiles with 1 meter spatial resolution) were used: Ecosystem Structure, Slope and Aspect.

The Ecosystem Structure data product is a Canopy Height Model (CHM) raster, essentially a surface of normalized vegetation heights, distributed in GeoTIFF format. The CHM is produced by separating discrete LiDAR returns into ground and vegetation classes [NEON.DOC.002387]. The ground returns are used to create a rasterized Digital Terrain Model (DTM), elevations describing the physical terrain or “bare earth”, while the vegetation returns are used to create a rasterized Digital Surface Model (DSM), elevations describing objects on top of the ground surface. Subtracting the DTM from the DSM yields a surface of ground-normalized vegetation height, containing artifacts known as “data pits”. Based on the pulse width of the outgoing laser pulse (10 ns), any object under two meters may potentially be confused with the ground, so all heights below 2 meters in the CHM are rounded down to a height of 0 meters. NEON implements an algorithm to remove data pits for a more accurate estimation of

canopy height. CHM data provide valuable tree structure information to supplement the spectral information from the other AOP instruments and better inform species classification efforts. The Slope and Aspect data products are derived from the DTM. Slope is determined as the angle between a plane tangential to the local terrain surface and a plane tangential to the local geoid surface, reported in degrees. Aspect is the direction of the steepest slope, given in degrees referenced to grid north.

2.2.3 Digital camera

The multispectral digital camera measures light reflected in the red, green, and blue (RGB) bands within the visible range of wavelengths. Across its multiple payloads, NEON operates two Phase One iXU-RS1000 (100 MP) aerial cameras, and one Phase One iXA (80 MP) camera. RGB 8-bit intensity is captured with a 10 cm spatial resolution in the “High-resolution orthorectified camera imagery mosaic” data product and distributed as multi-band GeoTIFF files [NEON.DOC.001211]. The digital camera imagery is remapped to the same geographic projection as the simultaneously captured LiDAR and imaging spectrometer data. The higher spatial resolution of the digital camera imagery can aid in identifying fine features such as boundaries of individual tree crowns in dense canopy that are not as visible in the other airborne data products. Figure 1 illustrates the differences in spatial resolution and also the type of information captured by each of the three NEON AOP instruments.

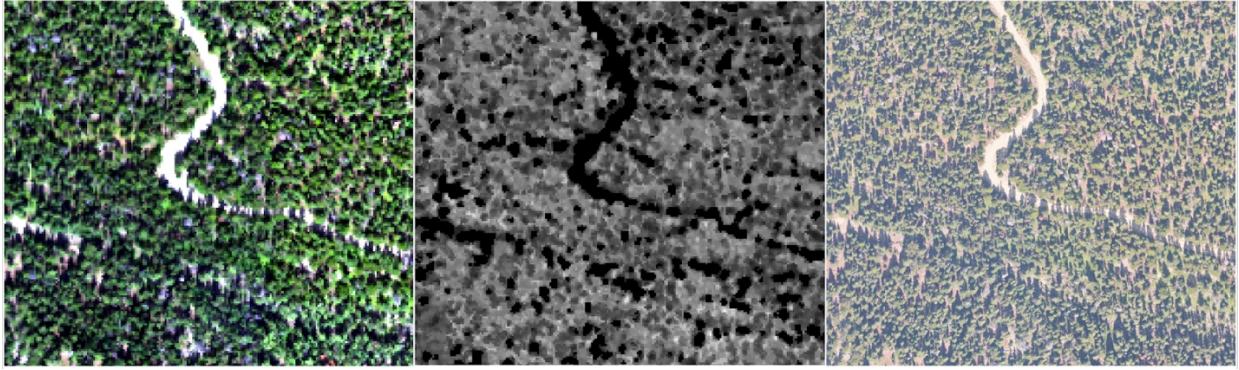


Figure 1: Comparison of spatial resolutions and information captured by the raster data products from each of the three AOP instruments: Hyperspectral true-color composite with 1m pixel size using NIS bands 450, 555, and 620 nm (left), discrete lidar-derived canopy height model with 1m pixel size, where black indicates ground and brighter pixels represent taller canopy height above ground (center), and digital camera RGB composite with 0.1m pixel size.

2.3 NEON field-based vegetation sampling methods

In-situ vegetation measurements are made in synchrony with NEON AOP imagery collections. The NEON Woody Plant Vegetation Structure data collection follows the Terrestrial Organismal Sampling (TOS) protocol for Measurement of Vegetation Structure [NEON.DOC.000987] at forested sites. Within a NEON site, there are a variety of plot types: Tower (located within the footprint of the instrumentation-mounted flux tower, each 40m x 40m in size), Distributed (between 20 and 50 plots distributed in a stratified random manner across the site, 20m x 20m in size), and Gradient (additional plots established as needed to capture major topographical, vegetation, or hydrologic gradients present). Tower plots are sampled annually while distributed plots have a 3-year sampling interval. Each distributed plot is sampled if at least one tree stem with diameter at breast height (DBH) ≥ 10 cm is located within the plot boundaries. Within a plot, all individual plants that exceed the DBH threshold are mapped and measured throughout the plot sampling area. For subplots containing only heterogeneously

distributed individuals with DBH < 10 cm, nested subplots ranging in size from 1m² to 100m² may be employed [NEON.DOC.000987].

Vegetation measurements collected using the TOS protocol include the location and species of tree stems, total stem height, crown diameter, and DBH. An offset mapping technique is used to determine the within-plot location of mapped stems relative to permanent plot markers where high-resolution GPS measurements have already been recorded. A laser rangefinder (\pm 30 cm accuracy) is used to measure the distance and azimuth of each stem relative to the permanent plot reference point. Crown diameter is also measured using the laser rangefinder, to the nearest 0.1m. DBH is measured using diameter tape or calipers. The species is determined by the field technician and the corresponding taxon ID code is recorded from a NEON master list of plant species. This taxon list provides codes for instances when identification below a specific taxonomic rank (such as family or genus) cannot be made.

Each measured stem is assigned a unique individual ID, which allows data entries to be matched across separate NEON data tables that contain mapped tree attributes. As the documentation describes, “One or more records expected for each tagged woody individual (individualID) for all time. Corrections to taxonID or mapped location through time will result in duplicate individual IDs. In the case of duplicates, users are advised to retain the record with the latest date.” Multiple records per individual ID are also created for multi-bole individuals (those with forked trunks that meet specific requirements), with a letter appended onto the end of the five-digit individual ID code (for example, “02013A”, “02013B”). In the case of many multi-bole entries in the described 2016 NIWO data set, there may be two or more individual ID entries that indicate multi-bole measurements but are otherwise identical (in particular, they have the same mapped coordinates, height, and maximum crown diameter).

At the NIWO site, distributed plots are measured using the vegetation structure protocol but tower plots are not, due to the fact that most of the tower airshed is above tree line. Pairing these *in-situ* ground truth measurements with remote sensing observations provides a promising opportunity to create a well-labeled data set to inform species classification efforts.

2.4 Tree species classification using remotely sensed data

2.4.1 Remote sensing features

The amount of studies utilizing remotely sensed data to classify tree species has grown exponentially in the recent decades (Fassnacht et al., 2016). Researchers are using a variety of passive and active sensor types, most commonly hyperspectral or imaging spectroscopy, multispectral imaging, and LiDAR, followed by synthetic aperture radar (SAR) systems. Many studies combine passive and active systems to capitalize on their strengths. Passive systems such as hyperspectral and multispectral cameras capture reflected light across a range of wavelengths, typically within the visible (VIS), near infrared (NIR) and shortwave infrared (SWIR) regions of the electromagnetic spectrum between approximately 400 and 2500 nanometers. The amount of light reflected by tree canopies across the VIS, NIR, and SWIR wavelengths is related to the plants' chemical properties, including pigments such as chlorophyll (Ustin et al., 2009), water content (Gao and Hoetz, 1990), leaf and crown structure, and health (Fassnacht et al., 2016). The VIS wavelengths, blue in particular, have been found to be especially useful for classifying conifer species (Pu and Liu, 2011). Many studies employ some form of feature reduction to efficiently condense or summarize data with many highly correlated bands, such as is the case with hyperspectral imagery, using methods such as principal component analysis (PCA) (Maschler et al., 2018). PCA projects the hyperspectral data into a new feature subspace with

uncorrelated principal components. Texture metrics are another form of feature reduction, as they quantify the spatial variation or patterns of image brightness values within a given region, such as a tree crown or stand. Texture metrics have been shown to improve species classification accuracies, especially when species exhibit characteristic crown structure and shadows (Franklin et al., 2000). Active remote sensing systems, such as LiDAR and SAR, capture information related to the height of vegetation, shape of tree crowns, and density or layering of canopies. Incorporating these types of structural data has been shown to improve species classification accuracies, especially when combined with passive data sets (Wang et al., 2019). Tree species classification accuracies reported throughout the literature vary widely from approximately 60% to 95%, along with the type and number of sensors used, biodiversity within forests, and classification methods utilized (Fassnacht et al., 2016).

2.4.2 Random forest classifier

One of the most commonly applied machine learning algorithms is Random Forest (RF), a non-parametric supervised classification method that uses an ensemble of decision trees, also known as “bootstrap aggregated” or “bagged” decision trees (Breiman et al., 2001). Each decision tree in the “forest” considers a random subset of features and only has access to a random set of the training data samples (approximately two-thirds of the collected data). The remaining one-third of the data is then used to predict upon using the previously created decision tree. Whereas using a single decision tree is known to lead to overfitting on the training set, building multiple decision trees by iteratively resampling data from the training set reduces the occurrence of overfitting for greater stability and accuracy. Each decision tree within the ensemble “votes” for a final outcome value and the class with the greatest number of votes is

assigned in the end. As a form of data-splitting, this Out-Of-Bag (OOB) bootstrap-resampling procedure can provide a reliable estimate of accuracy for unseen data, although a completely independent test set is recommended as the “a gold standard for tree species classification studies” (Fassnacht et al., 2016). There are two hyperparameters that may be tuned when constructing a RF classifier: the number of decision trees (ntree) and the number of variables sampled randomly as each split or stage to grow a single tree (mtry). One criterion used to rank predictor variable importance within the random forest classification is the Mean Decrease in Accuracy (MDA), where classification accuracy is calculated while excluding each single variable (Liu et al., 2017). When the greatest decrease in accuracy is observed, this indicates that a variable is the most important for classification. Assessing variable importance is a valuable step for feature selection and creating parsimonious models, which use the fewest predictor variables possible.

2.4.3 Accuracy assessment

A variety of metrics are used to assess the accuracy of a classification. Overall accuracy (OA) is calculated by dividing the total number of correctly classified reference samples by the total number of reference samples. OA is the complement of the OOB error estimate. Confusion matrices are used to compare the known classes of reference samples to their predicted classes after classification. Rows in the confusion matrix describe known reference sample classes and columns describe the predicted classes. The number of accurate predictions are tallied along the diagonal, where the reference class is the same as the predicted class. The number of misclassifications for each reference and predicted class combination are presented in the other

cells of the confusion matrix, from which errors of commission and omission can be calculated for each of the classes.

Errors of commission are the number of false positives, samples incorrectly classified in the target class. Errors of omission are the number of false negatives, samples incorrectly left out of the target class. User's and producer's accuracies describe accuracy of the resulting classification output from the perspective of the map consumer and creator, respectively.

Producer's accuracy (PA) is the complement of omission error. From the perspective of a map maker, PA quantifies the proportion of reference samples accurately assigned to the target class compared to the total number of reference samples for that class. User's accuracy (UA) is the complement of commission error. From the perspective of someone using the classification map, UA quantifies how often the target class on the map represents the target class on the ground, or in reality. Cohen's Kappa coefficient (K) is a statistic that evaluates classification performance, also known as "observed accuracy", compared to random chance or "expected accuracy". K ranges from 0 to 1; a value of 0 means that the classification is no better than random chance, while a value of 1 indicates a classification that is much better than random chance.

CHAPTER 3

METHODS

3.1 Study area

The area of study for this research is the Niwot Ridge Mountain Research Station (NIWO) NEON site located on the eastern slope of the Colorado Front Range (Figure 2). This site in the Southern Rockies is 27km west of Boulder, Colorado and 6km east of the Colorado Continental Divide. The Rocky Mountain ecosystems present here include alpine tundra and subalpine coniferous forests. Dominant tree species present within the subalpine coniferous forest plots at NIWO are presented in Table 1, along with the corresponding taxon codes for identification of each species recorded by NEON field technicians.

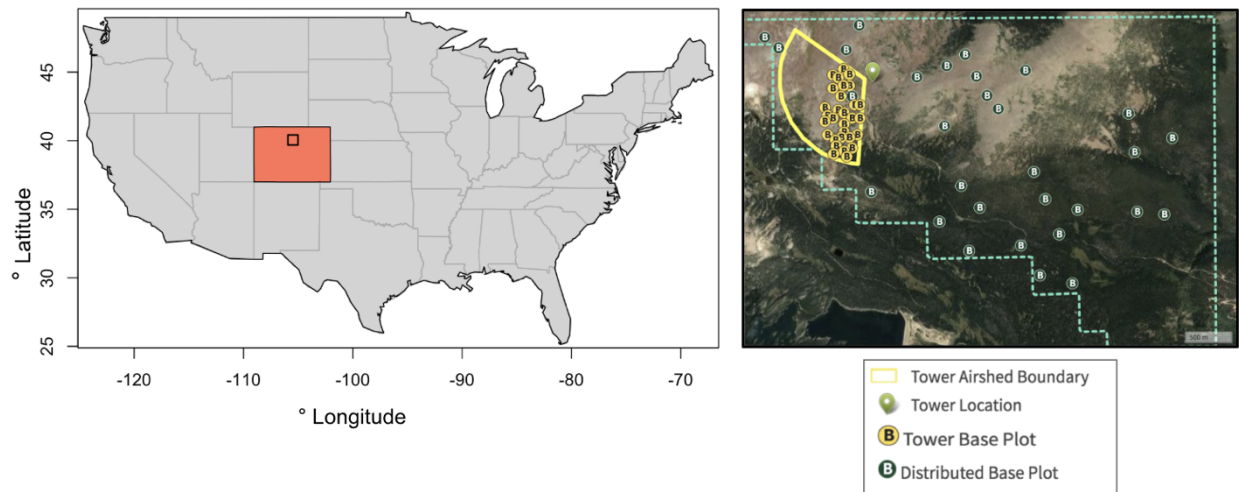


Figure 2: Location of the Niwot Ridge Mountain Research Station (NIWO) in NEON Domain 13, Southern Rockies & Colorado (left) and the extent of the NIWO site along with the location of various sampling plots (right). Airborne remote sensing data is collected across this region annually. Field-based tree measurements are collected at subplots throughout the site every 1-3 years, depending on plot type.

Table 1. Tree species present at the NIWO NEON site for all plots combined in the 2016 woody vegetation structure data.

Scientific Name	Common Name	Taxon ID	Number of mapped trees at NIWO
<i>Abies lasiocarpa</i>	Subalpine fir	ABLAL	249
<i>Pinus contorta</i>	Lodgepole pine	PICOL	112
<i>Picea engelmannii</i>	Engelmann spruce	PIEN	264
<i>Pinus flexilis</i>	Limber pine	PIFL2	74

3.2 NEON data

Woody vegetation structure data, along with selected AOP data products, were downloaded from the NEON Data Portal (<https://data.neonscience.org/>) for the NIWO site (Table 2). The most recent woody plant vegetation structure data available for download during the timeframe of this study was collected during August, extending through October of 2016, and consist of 699 trees with mapped stem locations and crown measurements (Table 1). The closest date of available airborne remote sensing data products was September 2017. All data products were downloaded during the summer and fall of 2018.

3.3 Reference data processing

The *in-situ* woody vegetation structure data includes tree locations and corresponding crown diameters. A series of reference data sets were generated to investigate their influence on species classification: tree stem point locations, circular polygons with the maximum crown diameter of each tree, and circular polygons with half of the maximum crown diameter of each tree to serve as an intermediate step between points and large polygons (Figure 3). Notice that

many of the points and polygons are overlapping, which means that multiple trees will be associated with individual pixel locations in the overlapping areas. Also notice that there are duplicate polygons present in some locations, which are generated as a result of multi-bole entries present in the reference data set. Tree crowns were modeled as circles in this study due to the lack of more specific crown shape measurements in the data set. It is understood that in reality, tree crowns at NIWO are often irregularly shaped and asymmetrical as a result to factors such as directional winds, sun exposure, and proximity of neighboring vegetation.

Table 2. Descriptions of NEON data downloaded for this study.

Sampling type	Data Product ID	Data Product Name	Date Collected
Terrestrial (<i>in-situ</i>)	NEON.DP1.10098.001	Woody plant vegetation structure	2016-08 - 2016-10
Airborne	NEON.DP3.30006.001	Spectrometer orthorectified surface directional reflectance - mosaic	2017-09
	NEON.DP3.30026.001	Vegetation indices - spectrometer - mosaic	
	NEON.DP3.30015.001	Ecosystem structure (CHM)	
	NEON.DP3.30025.001	Slope and Aspect - LiDAR	
	NEON.DP3.30010.001	High-resolution orthorectified camera imagery mosaic	

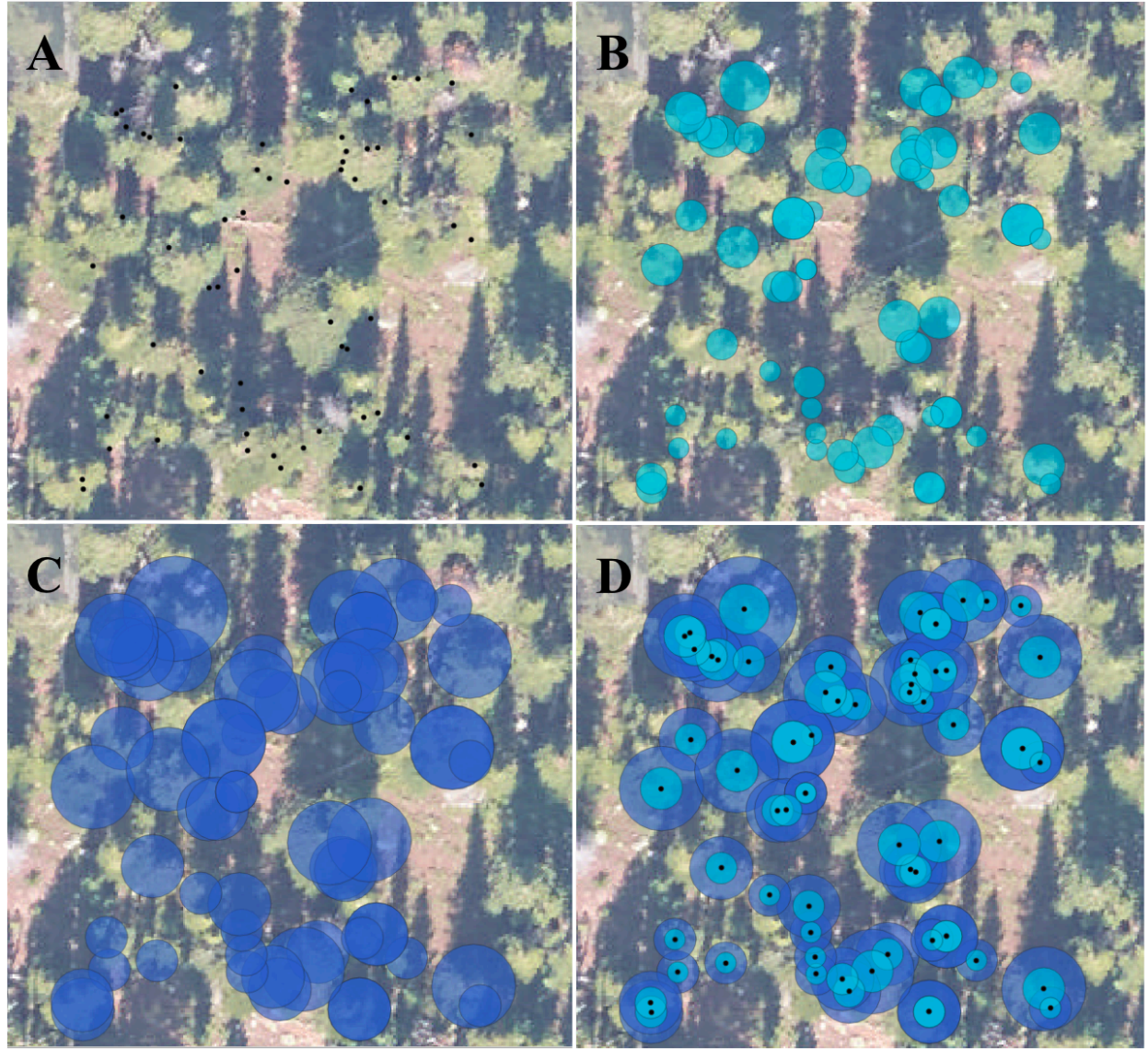


Figure 3: Reference data sets generated using all of the input woody vegetation measurements at the NIWO_015 distributed base plot with dimensions of 20 x 20m, located at 451146m East, 4432366m North. Tree stem points are shown in (A). Circular polygons with half the maximum crown diameter for each tree are shown in (B). Circular polygons created with the maximum crown diameter for each tree are shown in (C). All of these points and polygons are displayed together in (D). Polygons are displayed with 50% opacity to help illustrate the areas of overlap between adjacent polygons, as well as the presence of multi-bole entries which appear opaque where multiple identical polygons are present. The base layer is RGB image data collected by the AOP with 0.1m spatial resolution.

To investigate the potential value of processing these “raw” reference data, an experimental workflow was designed to remove small polygons and clip areas of overlap between adjacent polygons to preserve the taller trees, which are more likely visible from the airborne imagery. This open workflow, termed “neon_veg”, is being developed openly and collaboratively on GitHub (<https://github.com/earthlab/neon-veg>). In this workflow, identical multi-bole entries were identified and excluded from subsequent analysis to remove duplicated points or polygons present in the raw data set. An area threshold was then applied to remove any small trees with circular area values less than the area of four hyperspectral pixels. This threshold was employed with the coarser resolution of the hyperspectral and LiDAR data products in mind. By preserving the trees with larger crowns, it was believed that purer spectra would be extracted for them for the training data sets, as opposed to extracting mixed pixels which signal from smaller plants and background materials or neighboring vegetation. “Engulfed” polygons, those which are shorter and completely within the boundaries of other polygons, are also present in the initial reference data sets (Fig. 3). Since they likely cannot be observed from the airborne perspective, “engulfed” polygons were removed from subsequent analysis. Remaining polygons were checked for overlap with neighboring polygons. For each overlapping pair of polygons, shorter polygons were clipped by taller ones. If the remaining clipped area was smaller than the aforementioned area threshold, it was deleted. At this point, the workflow described has generated a collection of polygons that theoretically intersect with independent pixels in the airborne remote sensing data set (Figure 4).

The following six sets of reference data were used to evaluate species classification accuracy at the NEON NIWO site in this study: (1) points for all mapped tree stems, (2) polygons generated using the respective maximum crown diameter for all of the tree stems, (3)

polygons generated using half of the respective maximum crown diameter for all of the tree stems, (4) polygons with maximum tree crown diameter processed using the neon_veg workflow, (5) polygons with half of the maximum tree crown diameter processed using the neon_veg workflow, and (6) points for mapped tree stems (corresponding to the center locations of remaining polygons with maximum crown diameter) after being processed by the neon_veg workflow.

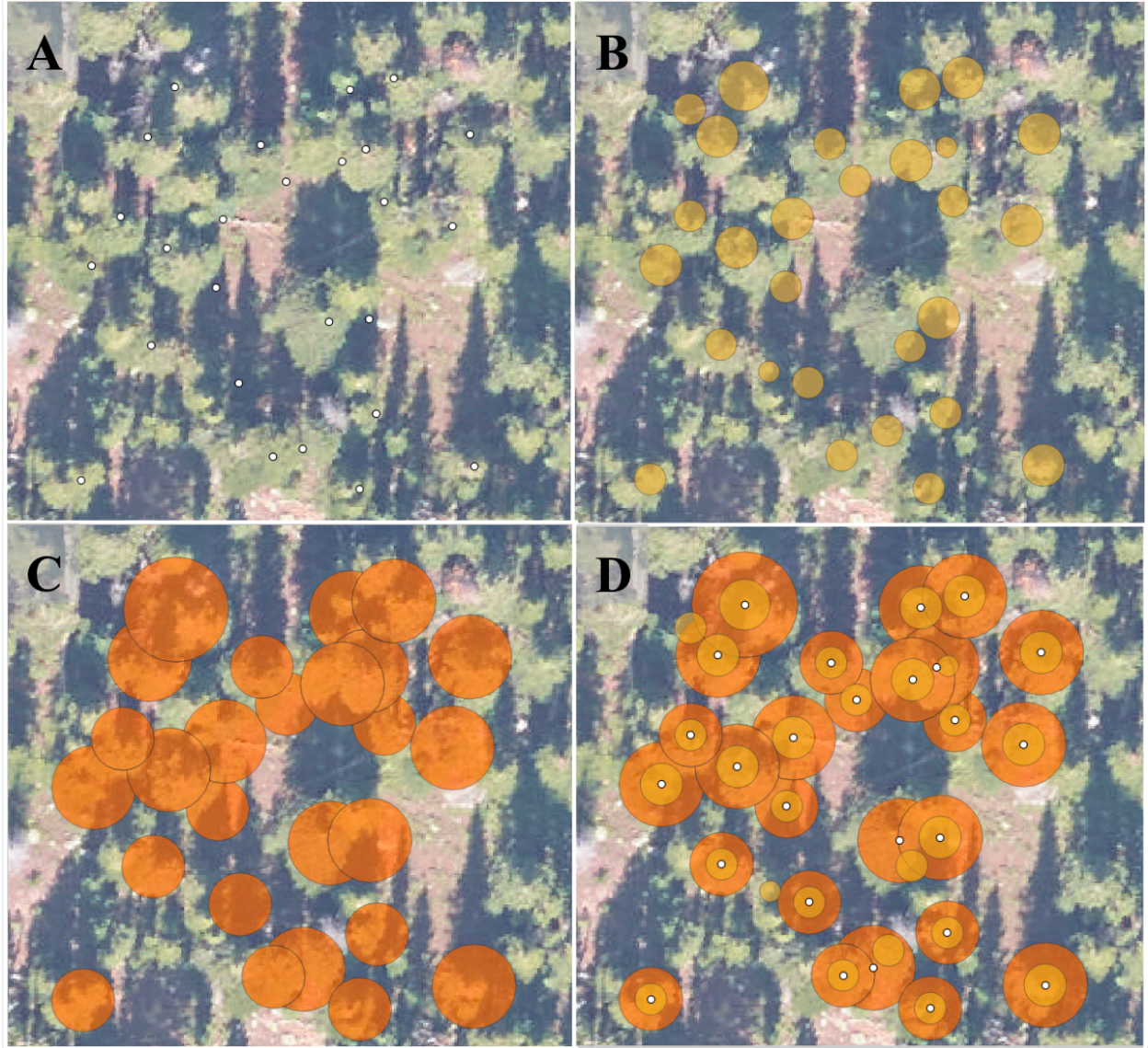


Figure 4: Reference data sets generated using the neon_veg workflow to filter out small tree crowns and clip overlapping crowns to preserve taller trees at the NIWO_015 distributed based plot. Tree stem points corresponding to the remaining polygons with maximum crown diameter are shown in (A). Circular polygons with half the maximum crown diameter for each tree are shown in (B). Circular polygons created with the maximum crown diameter for each tree are shown in (C). All of these points and polygons are displayed together in (D). Polygons are displayed with 50% opacity to help illustrate the areas of overlap between adjacent polygons. Note that there is no longer overlap between adjacent polygons, and multi-bole entries have been removed. The base layer is RGB image data collected by the AOP with 0.1m spatial resolution.

3.3 Feature extraction

To perform species classification, descriptive features must be extracted to explain the characteristics of each of the tree species at known reference locations in the remote sensing imagery. The NEON AOP-derived features that were utilized during this study describe the spectral, structural, and environmental characteristics of vegetation (Table 3). From the NIS, spectral reflectance at each of the individual bands were included to capture species-specific reflectance properties throughout the visible, near infrared, and shortwave infrared wavelengths. 372 individual wavelength bands remained after removing the “bad bands”, specified as 1340 to 1445 nm and 1790 to 1955 nm in the NIS metadata, where atmospheric water vapor absorbs light and leads to poor reflectance signal quality. To reduce the dimensionality of the hyperspectral data with many highly correlated bands, principal component analysis (PCA) was performed. PCA is a commonly used technique to transform large data sets with correlated dimensions into a new set of orthogonal dimensions or principal components. The first two principal components explained a cumulative proportion of 0.96 of the total variance, so the first two principal components (“PC1” and “PC2”) were extracted as a result and used as features, similarly as Liu et al. (2017). In addition to including the first two principal components, all seven of the Vegetation Indices calculated by NEON were included as descriptive features since they capture spectral differences between specific wavelengths that relate to vegetation health and chemical composition.

From multispectral digital camera imagery, the red, green, and blue (RGB) intensity bands were resampled from their 0.1m spatial resolution to match the 1m grid size of the other remote sensing products. Within each 1m by 1m grid cell, the aggregated mean and standard deviation of RGB intensities were calculated. The mean + standard deviation for each of the

RGB channels were included as features to capture the average spectral intensity in addition to the variation in intensity per pixel. The LiDAR-derived CHM provided height above ground at each pixel location. Although canopy height alone has limited value for species classification due to its dependence on individual tree age (Ghosh et al., 2014), it has been found to improve classification accuracies in some studies (Naidoo et al., 2012) and is useful for filtering non-canopy pixels in this exploratory study. The slope and aspect products describe the orientation and steepness of the underlying “bare earth” surface, which are important microclimate characteristics that influence species survival within a given environment (Walsh, 1980).

For each 1km by 1km tile, these airborne remote sensing data layers were combined into raster stacks. Any pixels with a height of 0 meters in the canopy height model were excluded, as they are assumed to contain signal from the ground. Each set of reference data was used to extract features from the remote sensing data stacks by determining which pixels intersect with each of the points or polygons. Each pixel was a sample described by the remote sensing-derived features.

Table 3. List and description of remote sensing-derived features used as training data in the Random Forest models for species classification.

Feature Name	Description	Formula / wavelengths used [nm]	Reference(s)
X381, X386, ... X2509	Spectral reflectance at each of the 426 bands (372 after removing bad bands)	381.3 - 2509.7 nm with 5 nm spacing	
*PC1, *PC2	1st and 2nd principal components		
*Vegetation Indices	Normalized Difference Vegetation Index (NDVI)	$NDVI = \frac{\lambda_{860} - \lambda_{650}}{\lambda_{860} + \lambda_{650}}$	(Rouse et al., 1974)
	Enhanced Vegetation Index (EVI)	$EVI = 2.5 \times \frac{\lambda_{860} - \lambda_{650}}{(\lambda_{860} + (6 \times \lambda_{650}) - (7.5 \times \lambda_{470}) + 1)}$	(Huete et al., 2002)
	Atmospherically Resistant Vegetation Index (ARVI)	$ARVI = \frac{\lambda_{860} - [\lambda_{650} - \gamma(\lambda_{470} - \lambda_{650})]}{\lambda_{860} + [\lambda_{650} - \gamma(\lambda_{470} - \lambda_{650})]}$	(Kaufman & Tanre, 1992)
	Canopy Xanthophyll, or Photochemical Reflectance Index (PRI)	$PRI = \frac{\lambda_{531} - \lambda_{570}}{\lambda_{531} + \lambda_{570}}$	(Gamon, Penuelas, & Field, 1992)
	Canopy Lignin, or Normalized Difference Lignin Index (NDLI)	$NDLI = \frac{\log(\frac{1}{\lambda_{1754}}) - \log(\frac{1}{\lambda_{1680}})}{\log(\frac{1}{\lambda_{1754}}) + \log(\frac{1}{\lambda_{1680}})}$	(Serrano, Penuelas, & Ustin, 2002)
	Normalized Difference Nitrogen Index (NDNI)	$NDNI = \frac{\log(\frac{1}{\lambda_{1510}}) - \log(\frac{1}{\lambda_{1680}})}{\log(\frac{1}{\lambda_{1510}}) + \log(\frac{1}{\lambda_{1680}})}$	(Serrano, Penuelas, & Ustin, 2002)
	Soil-Adjusted Vegetation Index (SAVI)	$SAVI = \frac{(1+L)(\lambda_{850} - \lambda_{650})}{(\lambda_{850} + \lambda_{650} + L)}$	(Huete 1988)
*CHM	Height of canopy above ground	Digital Surface Model (DSM) – Digital Terrain Model (DTM) with modified data pit filling algorithm	(Naidoo et al., 2012)
*Slope	Steepness of bare earth surface		(Walsh, 1980)
*Aspect	Compass direction of steepest slope		(Walsh, 1980)
*rgb_mean_sd_R *rgb_mean_sd_G *rgb_mean_sd_B	Mean plus standard deviation of red, green, blue digital camera multispectral image intensity		

Where λ_n is reflectance at the specified wavelength in units of nanometers, γ is a weighting constant based on aerosol type and atmospheric compensation for ARVI, L is a correction factor to account for different soil conditions for SAVI. Asterisks indicate which features were used in the final selected model.

3.4 Random forest classification

The randomForest function within the randomForest R package (Liaw and Wiener, 2002) was used to predict species (in this case, the “taxon ID” attribute was used as a categorical class label for each sample) using the spectral and structural features derived from the AOP data described in the previous section. Six random forest classifiers were trained, each using a different set of reference data. A random selection of 20% of the pixels within the neon_veg half diameter data were initially left out, and all six models were trained on the remaining data within each set. Each RF model was then used to predict species of the 20% independent validation set. Classifier performance was assessed based on internal OOB error estimates and overall accuracy of the independent validation set predictions. Confusion matrices were used to assess user’s and producer’s accuracies for each of the four species. Cohen’s Kappa coefficient was also calculated to take into account the possibility of classification accuracy by chance.

Note that as a result of the filtering and clipping operations, the neon_veg reference data sets contained less than half of the number of trees as the initial NEON data sets (Table 4). To test the potential influence of sampling bias on the classification results, three additional RF models were trained after reducing the number of trees for each “raw” data set to include the same tree IDs present in each corresponding neon_veg set. For instance, the 699 “all stem points” data set was filtered to consist of only the 266 stems that are present in the “neon_veg stem points” data set.

Table 4. Number of unique trees and pixels intersecting with each stem point or crown polygon across the six reference data sets. Unique trees were identified based on their “individualID” attribute in the *in-situ* NEON data. Unique pixels were identified based on their spatial location or coordinates within the scene.

Shapefile Description	Number of points or polygons	Number of pixels (extracted samples)
All stem points	699	554
All polygons, half diameter	699	1218
All polygons, max diameter	699	3005
Neon_veg stem points	266	266
Neon_veg polygons, half diameter	305	836
Neon_veg polygons, max diameter	266	2555

CHAPTER 4

RESULTS

Spectral reflectance curves were extracted from the 372 NIS hyperspectral bands for the points or polygons within each reference set (Appendix A). Spectral reflectance curves were extracted per species using all half-diameter polygons (Figure 5). As expected, the reflectance curves extracted per species using all half-diameter polygons appear very similar across the species with the characteristic green peak (~550 nm) within the visible wavelength region and the steep slope at the edge between the red and near infrared regions (~750 nm) and the shoulder or flattening off into the near infrared region (~800 nm). To compare reflectance magnitudes in different wavelength regions, all four mean spectral reflectance curves with standard deviation shading were overlaid (Appendix B). The overlaid mean reflectance curves extracted within all half-diameter polygons have very similar shapes across the conifer species but they appear to be biased or separated vertically to varying degrees (Figure 6). The relationship between reflectance magnitude across species curves differs across wavelength regions. For instance, *Abies lasiocarpa* (subalpine fir) has the highest mean spectral reflectance out of all the species from 400 to approximately 1300nm, but then *Pinus flexilis* (limber pine) has the highest mean spectral reflectance at all greater wavelengths out to 2500 nm (Figure 6). The mean spectral reflectance curves for *Pinus contorta* (lodgepole pine) and *Picea engelmannii* (Engelmann spruce) appear to be almost identical across all wavelengths, but there is a well-defined feature visible at approximately 1200nm where *Pinus contorta* mean reflectance drops sharply. Features and biases such as these may aid in differentiating between species during classification.

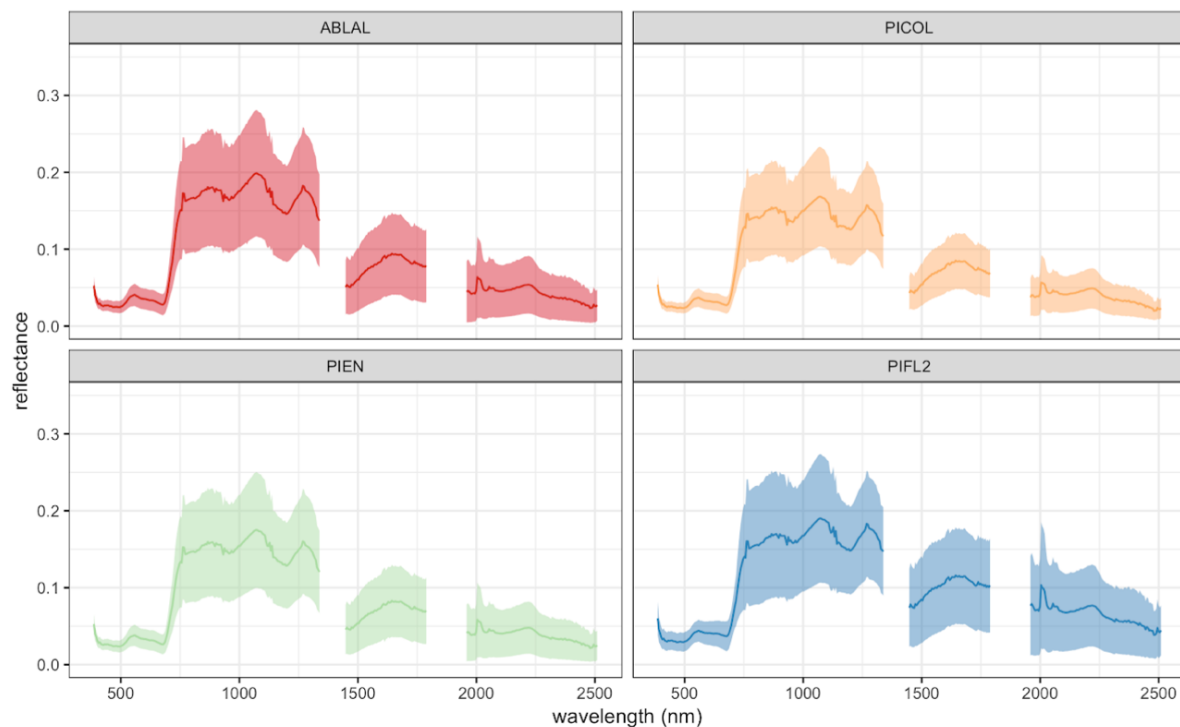


Figure 5: Mean spectral reflectance per species from 380 to 2510 nm, extracted from all polygons with half the max crown diameter at the NEON NIWO site for each of the dominant tree species: ABLAL (Subalpine fir), PICOL (Lodgepole pine), PIEN (Engelmann spruce), and PIFL2 (Limber pine). The shading illustrates \pm one standard deviation in reflectance per wavelength. Gaps in the spectra at approximately 1350 nm and 1800 nm are where “bad bands” were removed where there is high atmospheric absorption.

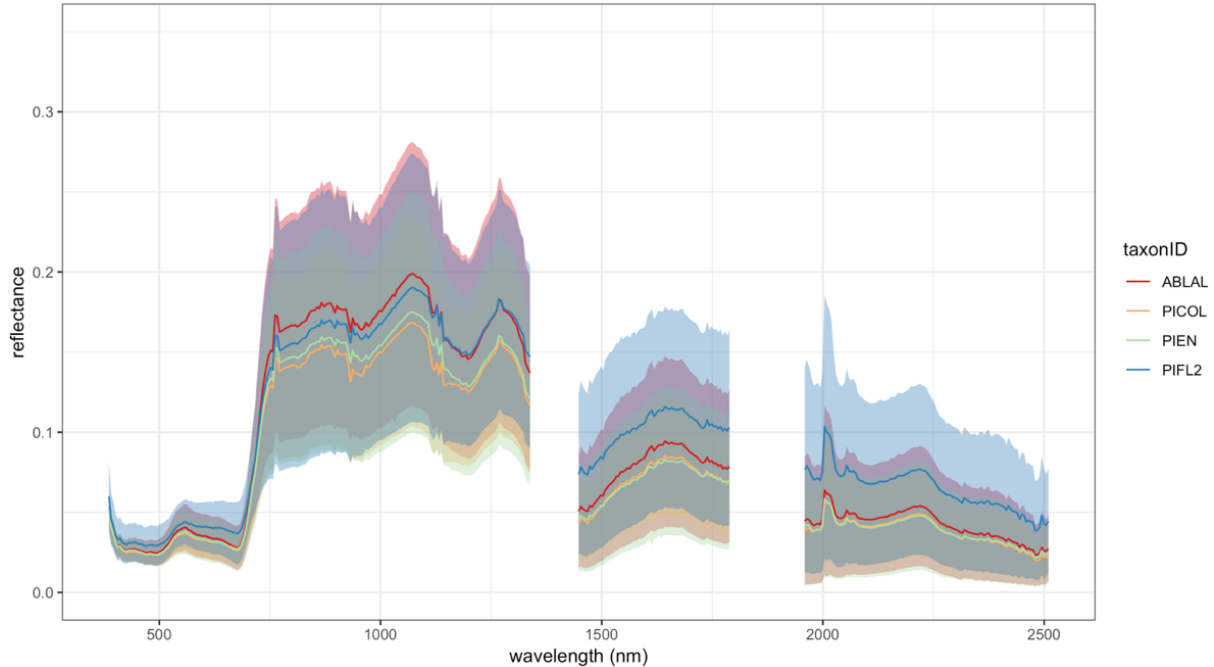


Figure 6: Mean spectral reflectance curves with shaded ± 1 standard deviation overlaid to compare reflectance magnitudes extracted from all polygons with half the maximum crown diameter across all four species: ABLAL (Subalpine fir), PICOL (Lodgepole pine), PIEN (Engelmann spruce), and PIFL2 (Limber pine).

Boxplots were generated to compare remote sensing-derived features across the tree species extracted for all polygons with half the maximum crown diameter (Figure 7). All 15 remote sensing-derived features were ranked in order of importance based on the Mean Decrease in Accuracy metric for all polygons compared with `neon_veg` polygons, each with half of the maximum crown diameter (Figure 8). Across all reference data sets, the structural features derived from the LiDAR data (aspect, slope, and canopy height) are ranked as the top three most important variables. This makes sense based on how these variables are depicted in the boxplots; their mean values and ranges appear to be well-separated across the four species. The importance of the remaining spectral variables is highly variable across reference sets with all points or polygons (Appendix C). For the `neon_veg` reference sets, the next most important variables

following the LiDAR-derived ones are vegetation indices (such as NDLI, ARVI, NDVI, PRI, in varying order).

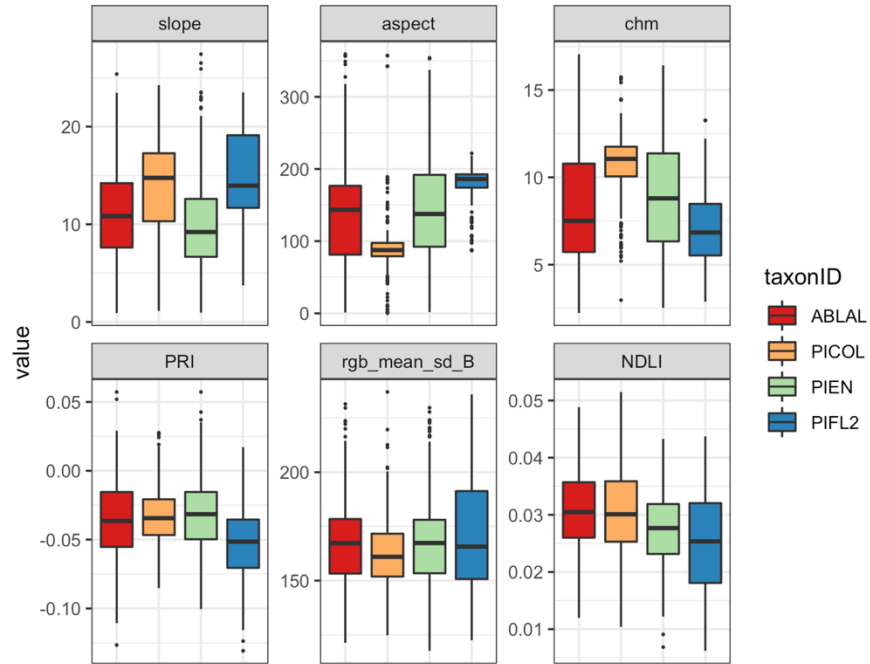


Figure 7: Interspecies comparison of remote sensing features extracted by all polygons with half of the maximum crown diameter. *Slope*, *aspect*, and *chm* (canopy height) are LiDAR-derived features. *PRI* (Photochemical Reflectance Index) and *NDLI* (Normalized Difference Lignin Index) are vegetation indices derived from the hyperspectral image data. *rgb_mean_sd_B* is the average plus standard deviation of intensity within each 1m grid cell derived from the multispectral digital camera imagery.

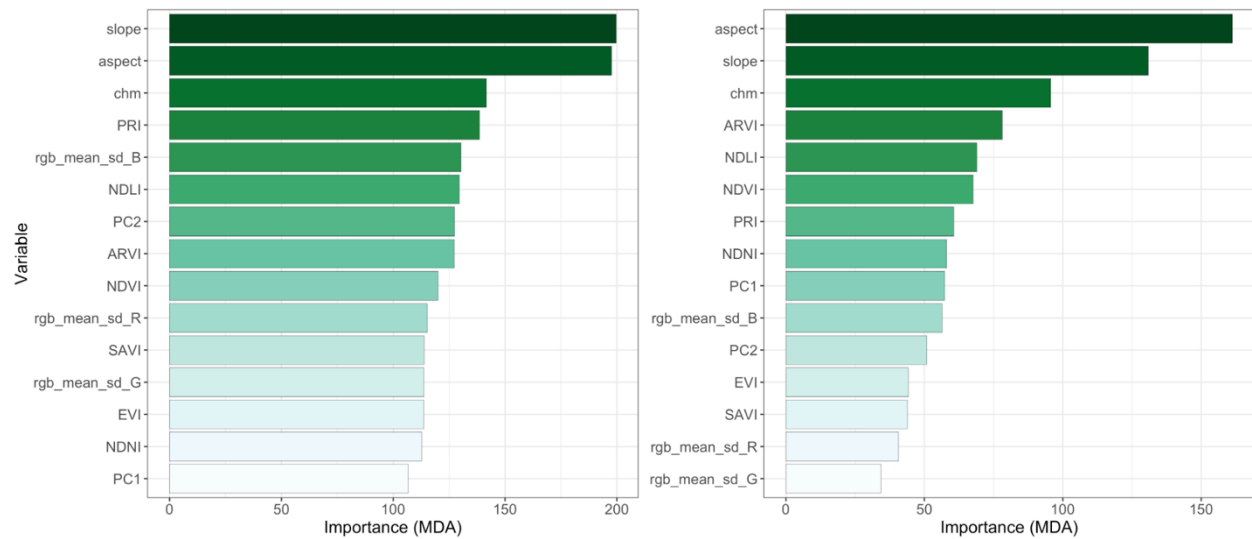


Figure 8. Predictor variable importance ranked by Mean Decrease in Accuracy (MDA) for Random Forest models trained using (A) all polygons with half the maximum crown diameter and (B) neon_veg polygons with half the maximum crown diameter. See Table 3 for remote sensing-derived variable definitions.

Overall classification results were compared for each of the RF models trained using all of the samples within each difference reference data set (Table 5). Based on OOB error, the training sets with all points and/or polygons yielded the highest overall accuracy (OA) values ranging from 70.1% for the tree stem points to 73.1% for the polygons with half-crown diameter. OA for the neon_veg data sets followed a similar pattern, with OA ranging from 61.0% to 68.3% for tree stem points and polygons with half diameter, respectively. The OA for max-diameter polygons fell somewhere in between for both cases. Based on the independent validation set, all polygons with half and max diameter yielded the highest OA of 68.5%. The next highest OA belonged to the half-crown diameter neon_veg polygons. This indicates that polygons created with half the maximum crown diameter yielded the highest OA, while using tree stem points performed the poorest based on OA.

Table 5. Overall classification results RF models using different reference sets for training. Bold text highlights row with the highest OA.

Reference data set	OA (%) OOB error	OA (%) Independent Validation	Kappa OOB
All stem points	70.1	56.2	0.563
All polygons, half diameter	73.1	68.5	0.629
All polygons, max diameter	71.2	68.5	0.607
Neon_veg stem points	61.0	54.3	0.441
Neon_veg polygons, half diameter	68.3	65.4	0.566
Neon_veg polygons, max diameter	67.4	63.0	0.545

After reducing the trees in each of the raw NEON datasets to match those trees within each of the corresponding neon_veg training datasets, the overall classification accuracies were compared (Table 6). This comparison was done to test the impact of the filtering and clipping operations within the neon_veg workflow, and to control for the stark difference in sample size (Table 4). The classification accuracies are now almost identical between each pair of corresponding reference set shapes (all vs. neon_veg points, all vs. neon_veg polygons with half diameter, all vs. neon_veg polygons with maximum crown diameter). Based on OOB error, the neon_veg half diameter polygons training set yielded the highest OA, 68.4%. The next highest OA based on OOB error was produced using all polygons with half diameter, 67.9%. Based on the independent validation set, all polygons with half diameter and max diameter both yielded the highest OA of 65.4%, followed closely by the neon_veg polygons with half diameter with an OA of 64.8%. Both training sets with tree stem points yielded the lowest OA values, approximately 61% and 55% based on OOB and independent validation, respectively.

Table 6. Overall classification results for each RF model using a different reference data set for training, but the tree IDs were reduced in each of the raw NEON datasets to match those within each of the corresponding neon_veg datasets. This reduces the sampling bias and allows for the clipping/filtering output to be compared with the raw reference datasets generated without any preprocessing. Bold text highlights row with the highest OA based on OOB error and independent validation.

Reference data set	OA (%) OOB error	OA (%) Independent Validation	Kappa OOB
All stem points	61.5	56.2	0.449
All polygons, half diameter	67.9	65.4	0.561
All polygons, max diameter	63.0	65.4	0.493
Neon_veg stem points	61.0	54.3	0.441
Neon_veg polygons, half diameter	68.4	64.8	0.568
Neon_veg polygons, max diameter	67.4	63.0	0.545

To compare the classification accuracies for each of the species present at the NIWO site, confusion matrices were calculated for the half diameter polygon datasets (Table 7). The user's and producer's accuracies varied greatly across the four species, from 42% at the worst to 87% at the best. *Pinus flexilis* (Limber pine) is consistently the most accurately classified species, while *Abies lasiocarpa* (Subalpine fir) is consistently the least accurately classified species. *Abies lasiocarpa* is often incorrectly predicted as *Picea engelmannii* (Engelmann spruce). This is interesting, as *Abies lasiocarpa* had the most mapped trees in the *in-situ* data set at NIWO whereas *Pinus flexilis* had the fewest.

Table 7. Confusion matrices with User's Accuracy (UA) and Producer's Accuracy (PA) per species for (A) all polygons with max-crown diameter, (B) neon_veg polygons with half-crown diameter, and (C) all polygons with half-crown diameter when the trees are reduced to those within the neon_veg set to assess the impact of reduced sample size.

A		Predicted				
		ABLAL	PICOL	PIEN	PIFL2	PA (%)
Reference	ABLAL	255	26	99	20	63.8
	PICOL	26	159	42	11	66.8
	PIEN	73	21	381	29	75.6
	PIFL2	13	1	23	248	87.0
	UA (%)	69.5	76.8	69.9	80.5	

B		Predicted				
		ABLAL	PICOL	PIEN	PIFL2	PA (%)
Reference	ABLAL	64	15	56	12	43.5
	PICOL	9	80	30	10	62.0
	PIEN	25	13	164	17	74.9
	PIFL2	5	0	14	136	87.7
	UA (%)	62.1	74.1	62.1	77.7	

C		Predicted				
		ABLAL	PICOL	PIEN	PIFL2	PA (%)
Reference	ABLAL	63	13	59	12	42.9
	PICOL	8	79	33	10	60.8
	PIEN	24	15	162	18	74.0
	PIFL2	5	0	13	141	88.7
	UA (%)	63.0	73.8	60.7	77.9	

CHAPTER 5

DISCUSSION

The aims of this study were to perform an initial tree species classification analysis at the NIWO NEON site, compare the accuracies resulting from different stem point and circular crown polygon training data sets, and evaluate which AOP remote sensing data raster products were most important for accurate species classification using Random Forest (RF) models. Our results show overall accuracy (OA) values ranged from 61% to 73% (Table 5) when using different multispectral, hyperspectral, and LiDAR-derived training data sets. These OA values fall within the reported range of 65-95% for studies utilizing combined sensor systems reviewed by Fassnacht et al. (2016). We found OA values were higher when all of the reference data points or polygons were used, as opposed to the filtered and clipped neon_veg reference data. This does not support our hypothesis in which the clipping and filtering steps would improve classification accuracy. The logic behind this hypothesis was that by removing small suppressed crowns and associating each pixel in the remote sensing imagery with only the dominant and likely visible trees, there would theoretically be purer, more separable spectra extracted to capture the spectral and structural differences between the species of interest. However, our initial results do not support this, which may be explained by the presence of mixed species composition within pixels. In the field, it is clear that tree crowns in these subalpine forest ecosystems are often irregularly shaped, overlapping with neighboring crowns, and have gaps that allow underlying materials to potentially be seen from the airborne perspective. Perhaps the association of multiple, overlapping points and polygons with a single pixel helps to describe the

mixed pixels in the training data sets where there is signal from the understory reaching the sensor.

Another potential explanation is the limited sample size of the neon_veg reference sets, which contain less than 50% of the trees present in the initial reference sets (Table 4). When the number of trees in the reference sets were reduced to match those within the neon_veg sets to compare the effect of the clipping and filtering operations, the overall accuracies between each set of points and polygons became almost identical, within 2-3% of one another (Table 6). This indicates that the smaller sample size has a substantial effect on classification results. When additional woody vegetation structure measurements are collected at NIWO in the future, it will be interesting to assess how the species classification results may change with an increased sample size.

The reported classification accuracies indicate that using polygons with half of the maximum crown diameter per tree is better than using stem point locations or polygons created with the maximum crown diameter per tree (Table 5; Table 6). This is useful information for future creation of training data, as the provided crown measurements available include stem point locations and maximum crown diameter. Minimum crown diameter measurements are also available would be interesting to test for modeling crown size. It is understood that tree crowns are rarely perfectly circular in reality.

Besides the filtering and clipping steps in the experimental neon_veg workflow and using the CHM to remove pixels associated with a canopy height of zero, the points and circular polygons derived from the *in-situ* tree measurements were utilized entirely as-is in this study without any quality assessment or alignment procedures. It is evident that some stem locations and polygons extend beyond the actual location of tree crowns (Figure 3). This is potentially a

result of field measurement errors as well as georectification and image formation artifacts introduced during the creation of the remote sensing data products. Also, this study performed pixel-based classification for simplicity and initial exploration, but a variety of studies across the current literature are experimenting with manual and automated tree crown delineation to refine the selection of pixels within their reference data sets and perform object-based classification (Koch et al., 2013; Graves et al., 2018). Beyond using the CHM to identify canopy pixels, additional spectral criteria can be utilized such as applying an NDVI threshold to isolate forest pixels and eliminate shadow pixels (Maschler et al. 2018). An NDVI threshold could also be used to identify pixels with trees that have died since the collection of the field data, as there was a time difference of one year between the *in-situ* and remote sensing data collections in this study. Incorporating additional steps to refine the reference data sets, ensure alignment with the remote sensing imagery, and delineate individual crown boundaries instead of assuming perfectly circular crowns will likely improve upon the accuracies achieved here.

This study utilized a series of remote sensing raster data products generated by NEON from all three AOP instruments. The variable importance assessment shows that the LiDAR-derived remote sensing features were consistently ranked as the most important for species classification (Figure 8). Aspect and slope are understood to be important drivers of microclimate conditions such as temperature, moisture, sun and wind exposure, so their importance has ecological merit in the mountainous landscape of the Southern Rockies. However, as described in Fassnacht et al. (2016), canopy height, on its own, is limited for robust species classification as it is dependent on tree age. In addition to using the CHM, other studies have found that calculating metrics related to the vertical distribution, density and intensity of individual LiDAR returns improved classification results, so these metrics may be promising to

incorporate in the future (Alonzo et al., 2014). Future iterations of this work should calculate LiDAR point cloud-based metrics per pixel and/or tree crown object for improved species classifications.

Following the LiDAR-derived variables, the ranking of variable importance varied greatly between reference data sets. There is an interesting difference in the rate of variable importance falloff (Appendix D), where the variable importance plateaus after slope and aspect for the reference sets using all points or polygons. This means that there is not a substantial difference in variable importance, aside from aspect and slope, for these reference data. In contrast, the variable importance MDA values taper off more slowly for the *neon_veg* reference sets, which indicate a more meaningful ranking beyond the LiDAR-derived variables as a result of the filtering and clipping operations within the *neon_veg* workflow. The vegetation indices were generally found to be more important than the multispectral intensity metrics when the *neon_veg* reference sets are used for training the RF models. These variable importance rankings would be useful for iterative variable selection in future classification efforts, such as how Maschler et al. (2018) perform backwards feature selection. Starting with all input remote sensing features, variable importance was calculated and the single variable with the lowest MDA was removed from the next iteration of model training until a target OOB accuracy was reached. In addition, the RF model parameters were kept consistent across the models and a sensitivity analysis would be valuable to fine-tune parameters in subsequent analyses to potentially achieve higher species classification accuracies.

Since the *in-situ* and remote sensing data are collected following standardized sampling protocols across the United States, this method can be applied at other NEON sites to generate additional training data sets for regional species classification. However, the types of vegetation

and topography vary greatly across NEON domains, and we expect this to influence the resulting variable importance rankings and species classification accuracies. For instance, the LiDAR-derived features of slope and aspect describe the underlying terrain steepness and orientation. These two variables were found to be the important for species classification at the mountainous NIWO site in the Southern Rockies during this preliminary analysis. However, the Ordway-Swisher Biological Station (OSBS) site in north-central Florida has relatively flat terrain. We do not expect the slope and aspect variables to be as important for species classification at a site such as OSBS where slope and aspect are relatively constant across space. We anticipate that canopy height in addition to hyperspectral-derived features will be more important instead. Overall species classification is likely to be influenced by the diversity and tree canopy complexity at different ecosystems across NEON sites. For instance, San Joaquin Experimental Range (SJER) in central California features open woodland dominated by oak trees, pine trees, and scattered shrubs and grasses. Harvard Forest (HARV) in Massachusetts features primarily closed-canopy mixed forest composed of both coniferous and hardwood trees, densely packed with overlapping crowns. We expect greater species classification accuracies to be achieved at SJER compared to at HARV, since an open woodland offers simpler canopy structure and clearer separation between neighboring tree crowns. In addition, open woodland enables more accurate GPS measurements to be collected at plot corner locations as opposed to in dense, closed-canopy tree cover.

By applying this method across wider geographic extents and taking advantage of the long-term monitoring efforts of the NEON project, we are making strides towards answering ecological questions related to post-disturbance forest recovery. These airborne data provide a valuable intermediate step along the vertical column of observations from ground-based to

space-borne systems. We, as the ecological scientific community, will need to connect and supplement species composition estimates at the airborne scale with those from drones, to capture species characteristics and disturbance events that exist beyond NEON site boundaries. By linking these observations to those from satellite systems, we can extend our monitoring efforts into the global coverage and valuable historical record being collected over the past four decades. Studying how species composition shifts over time in response to different types and combinations of natural and anthropogenic disturbances will inform our understanding of future forest form and function.

CHAPTER 6

CONCLUSIONS

In this work, a series of reference data sets was created using NEON *in-situ* tree measurements and each one was used to train a pixel-based Random Forest (RF) model to classify tree species at the NIWO subalpine site. The highest classification accuracies, 73% and 68% based on internal OOB error and an independent validation set, respectively, were achieved using polygons created with half the maximum crown diameter per tree. The LiDAR-derived raster data products of aspect, slope, and canopy height were found to be the most important AOP remote sensing data-derived features, generally followed by vegetation indices. Applying the classifier to the entire NIWO site and assessing the output species map will add additional insight and meaning to these initial findings. Refining the reference data alignment with remote sensing imagery, incorporating additional variables from the LiDAR point cloud, and performing object-based classification on crown segments, rather than individual pixels, are all promising directions for subsequent analyses at NIWO. Scaling this species classification method to other NEON sites will also be informative of the proposed workflow's robustness. Connecting these airborne species classification observations with those from drones and satellites will extend the spatial and temporal reaches of this work in the future as well. This study contributes to the growing body of literature and open science that integrates NEON *in-situ* and airborne remote sensing data to map vegetation and study the effects of forest disturbances within diverse ecosystems across the United States.

REFERENCES

- Anderson, J.E., Plourde, L.C., Martin, M.E., Braswell, B.H., Smith, M.L., Dubayah, R.O., Hofton, M.A., Blair, J.B., 2008. Integrating waveform lidar with hyperspectral imagery for inventory of a northern temperate forest. *Remote Sens. Environ.* 112, 1856e1870
- Alonzo, M., Bookhagen, B., Roberts, D.A., 2014. Urban tree species mapping using hyperspectral and lidar data fusion. *Remote Sens. Environ.* 148, 70–83.
- Asner, G. P., Knapp, D. E., Boardman, J., Green, R. O., Kennedy-Bowdoin, T., Eastwood, M., ... Field, C. B. (2012). Carnegie Airborne Observatory-2: Increasing science data dimensionality via high-fidelity multi- sensor fusion. *Remote Sensing of the Environment*, 124, 454–465.
- Asner, G. P., R. E. Martin, D. E. Knapp, R. Tupayachi, C. B. Anderson, F. Sinca, N. R. Vaughn, and W. Llactayo. 2017. “Airborne Laser-Guided Imaging Spectroscopy to Map Forest Trait Diversity and Guide Conservation.” *Science* 355 (6323): 385.
<https://doi.org/10.1126/science.aaj1987>.
- Bentz, B.J., Régnière, J., Fettig, C.J., Hansen, E.M., Hayes, J.L., Hicke, J.A., Kelsy, R.G., Negrón, J.F., Seybold, S.J., 2010. Climate change and bark beetles of the western United States and Canada: direct and indirect effects. *Bioscience* 60, 602–613.
<http://dx.doi.org/10.1525/bio.2010.60.8.6>.
- Bonan, G.B. (2008). Forests and climate change: forcings, feedbacks, and the climate benefit of forests. *Science*, 320, 1444–1449.
- Breiman, L. (2001). Random forests. *Machine learning*, 45(1), 5-32.
- Buma, B. (2015). Disturbance interactions: characterization, prediction, and the potential for cascading effects. *Ecosphere*, 6. art.70
- Carpenter, J. May the best analyst win. *Science*, 331(6018):698–699, 2011.
- Coops, N. C., Wulder, M. A., Culvenor, D. S., & St-Onge, B. (2004). Comparison of forest attributes extracted from fine spatial resolution multispectral and lidar data. *Canadian Journal of Remote Sensing*, 30(6), 855–866. <https://doi.org/10.5589/m04-045>
- Dalponte, M., Bruzzone, L., & Gianelle, D. (2008). Fusion of hyperspectral and LiDAR remote sensing data for classification of complex forest areas. *IEEE Transactions on Geoscience and Remote Sensing*, 46, 1416–1427.
- Fassnacht, F. E., Latifi, H., Stereńczak, K., Modzelewska, A., Lefsky, M., Waser, L. T., ... & Ghosh, A. (2016). Review of studies on tree species classification from remotely sensed data. *Remote Sensing of Environment*, 186, 64-87.

Franklin, S.E., Hall, R.J., Moskal, L.M., Maudie, A.J., Lavigne, M.B., 2000. Incorporating texture into classification of forest species composition from airborne multispectral images. *Int. J. Remote Sens.* 21 (1), 61–79.

Gamon, J., J. Penuelas, and C. Field. "A Narrow-Waveband Spectral Index That Tracks Diurnal Changes in Photosynthetic Efficiency." *Remote Sensing of Environment* 41 (1992): 35-44.

Gao, B.C., Hoetz, A.F.H., 1990. Column atmospheric water-vapor and vegetation liquid water retrievals from airborne imaging spectrometer data. *J. Geophys. Res.-Atmos.* 95, 3549–3564.

Ghosh, A., Fassnacht, F.E., Joshi, P.K., Koch, B., 2014. A framework for mapping tree species combining hyperspectral and LiDAR data: Role of selected classifiers and sensor across three spatial scales. *Int. J. Appl. Earth Obs. Geoinf.* 26, 49–63.

Graves, S., Gearhart, J., Caughlin, T. T., & Bohlman, S. (2018). A digital mapping method for linking high-resolution remote sensing images to individual tree crowns. *PeerJ Preprints*, 6, e27182v1.

Greenwood, Sarah, Paloma Ruiz-Benito, Jordi Martínez-Vilalta, Francisco Lloret, Thomas Kitzberger, Craig D. Allen, Rod Fensham, et al. 2017. "Tree Mortality across Biomes Is Promoted by Drought Intensity, Lower Wood Density and Higher Specific Leaf Area." *Ecology Letters* 20 (4):539–53. <https://doi.org/10.1111/ele.12748>

Hansen, M. C., Potapov, P. V., Moore, R., Hancher, M., Turubanova, S. A., Tyukavina, A., . . . Kommareddy, A. (2013). High-resolution global maps of 21st-century forest cover change. *Science*, 342, 850–853.

Holling, C. S. 1973. Resilience and stability of ecological systems. *Annu Rev Ecol Syst* 4: 1–23.

Huete, A.R., 1988: A Soil-adjusted Vegetation Index (SAVI). *Remote Sensing of Environment*, 25(3): 295–309. DOI: 10.1016/0034-4257(88)90106-X.

Huete, A., et al. "Overview of the Radiometric and Biophysical Performance of the MODIS Vegetation Indices." *Remote Sensing of Environment* 83 (2002):195–213.

Kaartinen, H., Hyypä, J., Yu, X., Vastaranta, M., Hyypä, H., Kukko, A., . . . Wu, J. C. (2012). An international comparison of individual tree detection and extraction using airborne laser scanning. *Remote Sensing*, 4(4), 950–974. <https://doi.org/10.3390/rs4040950>

Kampe, T. U., Johnson, B. R., Kuester, M. K., and Michael Keller (2010). NEON: the first continental-scale ecological observatory with airborne remote sensing of vegetation canopy biochemistry and structure. *Journal of Applied Remote Sensing*, 4(1), 43510. <https://doi.org/10.1117/1.3361375>

Kaufman, Y., and D. Tanre. "Atmospherically Resistant Vegetation Index (ARVI) for EOS-MODIS. IEEE Transactions on Geoscience and Remote Sensing 30, no. 2 (1992): 261-270.

Keller M, Schimel DS, Hargrove WW, Hoffman FM. 2008. A continental strategy for the National Ecological Observatory Network. *Frontiers in Ecology and the Environment* 6(5):282-284

Koch, B., Kattenborn, T., Straub, C., Vauhkonen, J., 2013. Segmentation of forests to tree objects. In: Maltamo, M., Naesset, E., Vauhkonen, J. (Eds.), *Forestry Applications of Air-borne Laser Scanning*. Springer.

Liaw, A.; Wiener, M. Classification and regression by randomForest. *R News* 2002, 2/3, 18–22.

Liu, L.; Coops, N.C.; Aven, N.W.; Pang, Y (2017). Mapping urban tree species using integrated airborne hyperspectral and LiDAR remote sensing data. *Remote Sens. Environ.* 200, 170–182.

Marconi S, Graves SJ, Gong D, Nia MS, Le Bras M, Dorr BJ, Fontana P, Gearhart J, Greenberg C, Harris DJ, Kumar SA, Nishant A, Prabardh J, Rege SU, Bohlman SA, White EP, Wang DZ. 2019. A data science challenge for converting airborne remote sensing data into ecological information. *PeerJ* 6:e5843 <https://doi.org/10.7717/peerj.5843>

Maschler, J., Atzberger, C., & Immitzer, M. (2018). Individual Tree Crown Segmentation and Classification of 13 Tree Species Using Airborne Hyperspectral Data. *Remote Sensing*, 10(8), 1218.

Michener WK. 2015. Ecological data sharing. *Ecological Informatics* 29:33-44

Naidoo, L., Cho, M.A., Mathieu, R., Asner, G. (2012). Classification of savanna tree species, in the Greater Kruger National Park region, by integrating hyperspectral and LiDAR data in a random forest data mining environment. *ISPRS J. Photogramm. Remote Sens.* 69, 167–179. <http://dx.doi.org/10.1016/j.isprsjprs.2012.03.005>.

NEON.DOC.000987. (2017). *TOS Protocol and Procedure: Measurement of Vegetation Structure*. Revision G. Accessed from <https://data.neonscience.org/documents> on Jan 25, 2019.

NEON.DOC.001211. (2015). *NEON Algorithm Theoretical Basis Document (ATBD) - AOP Digital Camera Image Orthorectification*. Revision A. Accessed from <https://data.neonscience.org/documents> on Jan 25, 2019.

NEON.DOC.001288. (2015). *NEON imaging spectrometer radiance to reflectance algorithm theoretical document*. Revision A. Accessed from <https://data.neonscience.org/documents> on Jan 25, 2019.

NEON.DOC.002387. (2016) Neon ecosystem structure (canopy height model) algorithm theoretical basis document. Revision 1. Soon to be available from <https://data.neonscience.org/documents>.

NEON.DOC.002391. *NEON NDVI, EVI, Canopy Xanthophyll Cycle, and Canopy Lignin Algorithm Theoretical Basis Document*. (2016). Revision A. Accessed from <https://data.neonscience.org/documents> on Jan 25, 2019.

Paine, R. T., M. J. Tegner, and E. A. Johnson. 1998. Compounded perturbations yield ecological surprises. *Ecosystems* 16:535–545.

Pickett, S.T.A., and White, P.S., 1985. *The Ecology of Natural Disturbance and Patch Dynamics*. Academic Press Inc., Orlando, FL.

Pu, R. and D. Liu. 2011. Segmented canonical discriminant analysis of in situ hyperspectral data for identifying 13 urban tree species. *Int. J. Remote Sens.* 32 (8), 2207–2226.

Rouse, W., Haas, R.H., Deering, D.W., 1974. Monitoring vegetation systems in the Great Plains with ERTS. *NASA Spec. Publ.* 351, 309.

Scheffer M, Carpenter S, Foley J, et al. 2001. Catastrophic shifts in ecosystems. *Nature* 413: 591–96.

Schimel, D., & Keller, M. (2015). Big questions, big science: meeting the challenges of global ecology. *Oecologia*, 177(4), 925–934. <https://doi.org/10.1007/s00442-015-3236-3>

Seidl, Rupert, Dominik Thom, Markus Kautz, Dario Martin-Benito, Mikko Peltoniemi, Giorgio Vacchiano, Jan Wild, et al. 2017. “Forest Disturbances under Climate Change.” *Nature Climate Change* 7 (May): 395.

Serrano, L., J. Penuelas, and S. Ustin. "Remote Sensing of Nitrogen and Lignin in Mediterranean Vegetation from AVIRIS Data: Decomposing Biochemical from Structural Signals." *Remote Sensing of Environment* 81 (2002): 355-364.

Simard M, Romme WH, Griffin JM, and Turner MG. 2011. Do mountain pine beetle outbreaks change the probability of active crown fire in lodgepole pine forests? *Ecol Monogr* 81: 3–24.

Stavros, E. Natasha, David Schimel, Ryan Pavlick, Shawn Serbin, Abigail Swann, Laura Duncanson, Joshua B. Fisher, et al. 2017. “ISS Observations Offer Insights into Plant Function.” *Nature Ecology & Evolution* 1 (June): 0194.

Turner M (2005). Landscape ecology: what is the state of the science. *Annu Rev Ecol Syst* 36: 319–344.

Ustin, S., Gitelson, A.A., Jacquemoud, S.M., Asner, G.P., Gamon, J., Zarco-Tejada, 2009. Retrieval of foliar information about plant pigment systems from high resolution spectroscopy. *Remote Sens. Environ.* 113, 67–77.

Walsh, S.J., 1980. Coniferous tree species mapping using LANDSAT data. *Remote Sens. Environ.* 9 (1), 11–26.

Wang, K., Wang, T., & Liu, X. (2019). A Review: Individual Tree Species Classification Using Integrated Airborne LiDAR and Optical Imagery with a Focus on the Urban Environment. *Forests*, 10(1), 1.

Watson, James E. M., Tom Evans, Oscar Venter, Brooke Williams, Ayesha Tulloch, Claire Stewart, Ian Thompson, et al. (2018). “The Exceptional Value of Intact Forest Ecosystems.” *Nature Ecology & Evolution* 2 (4): 599–610. <https://doi.org/10.1038/s41559-018-0490-x>.

Westerling, A. L., H. G. Hidalgo, D. R. Cayan, and T. W. Swetnam. 2006. Warming and earlier spring increase western US forest wildfire activity. *Science* 313(5789):940–943.

APPENDIX

Appendix A. Spectral reflectance curves extracted per species

Mean spectral reflectance per species from 380 to 2510 nm, extracted for each set of reference data points or polygons the NEON NIWO site. The shading illustrates +/- one standard deviation in reflectance per wavelength. Gaps in the spectra at approximately 1350 nm and 1800 nm are where “bad bands” were removed where there is high atmospheric absorption.

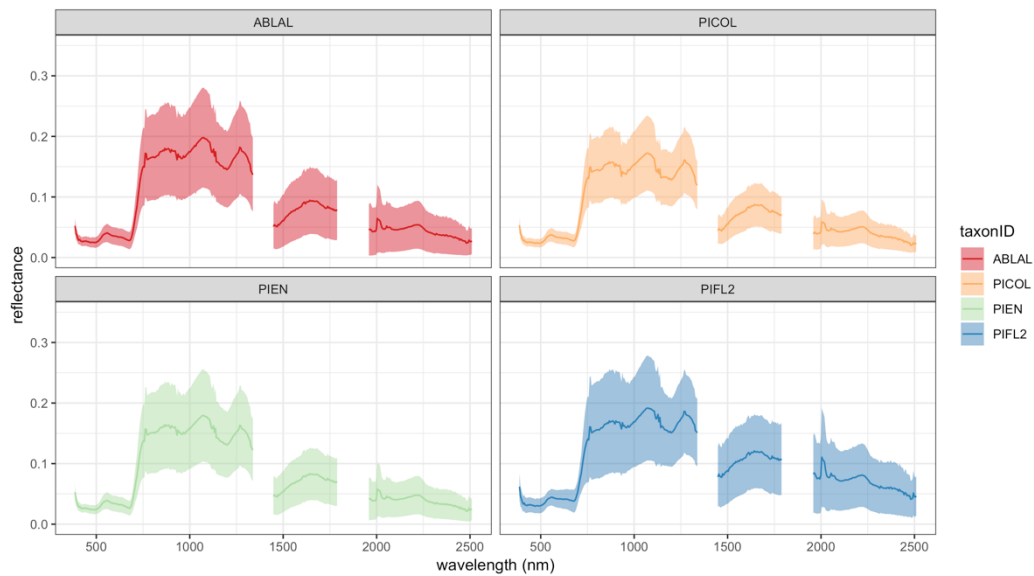


Figure A1: Mean spectral reflectance per species extracted from all tree stem points.

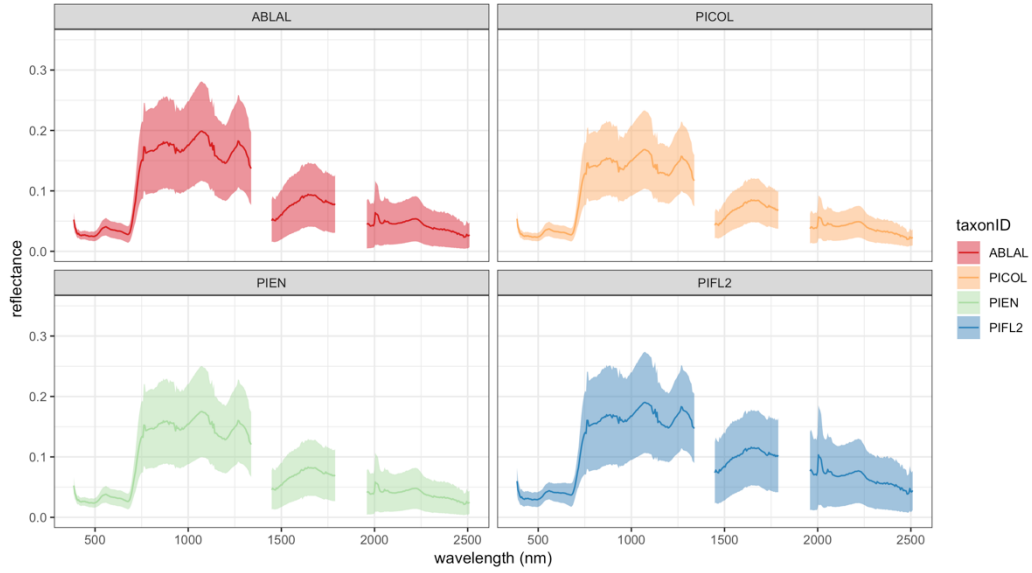


Figure A2: Mean spectral reflectance per species extracted from all half-diameter polygons.

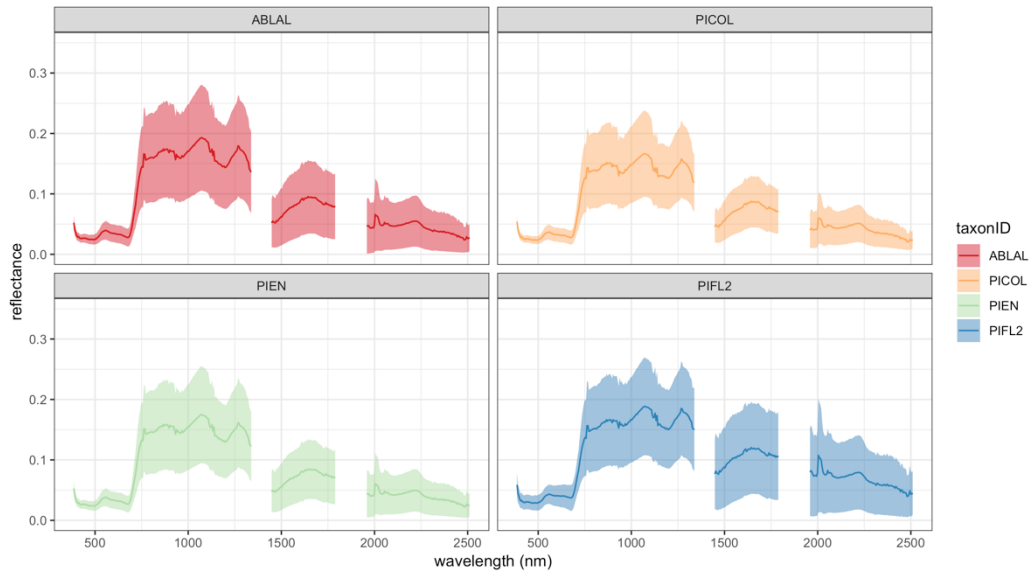


Figure A3: Mean spectral reflectance per species extracted from all max-diameter polygons.

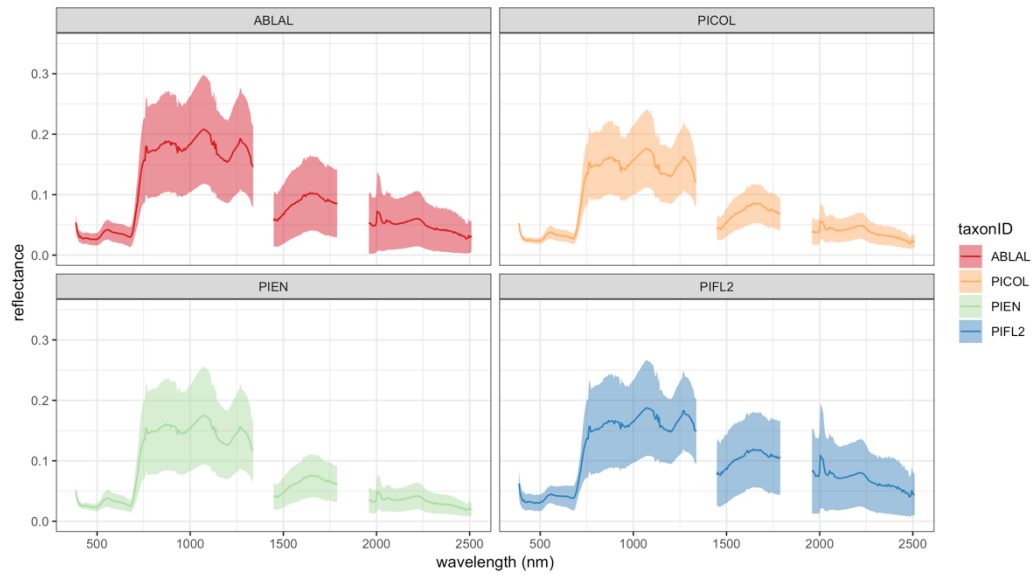


Figure A4: Mean spectral reflectance per species extracted from neon_veg tree stem points.

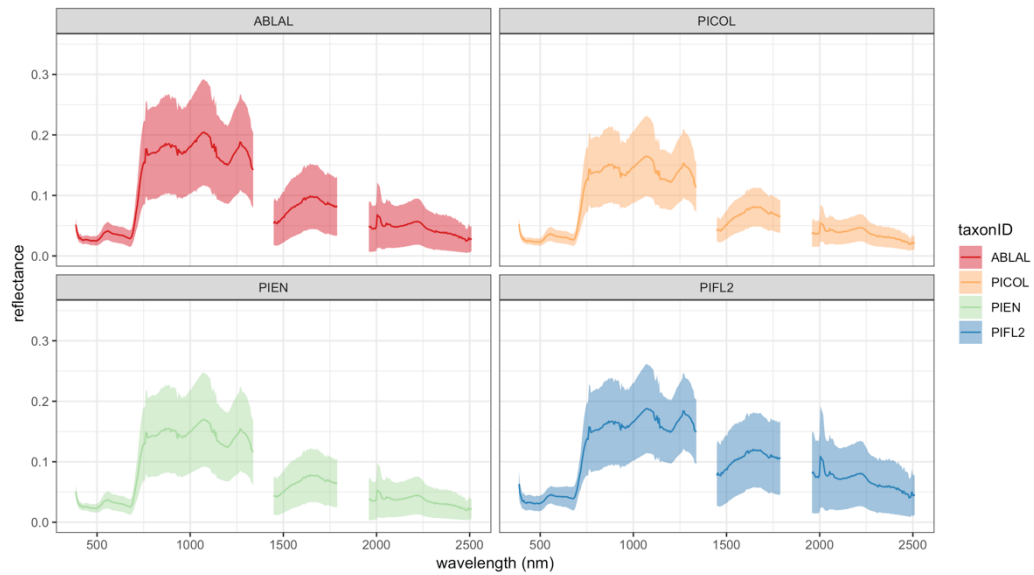


Figure A5: Mean spectral reflectance per species extracted from neon_veg half-diameter polygons.

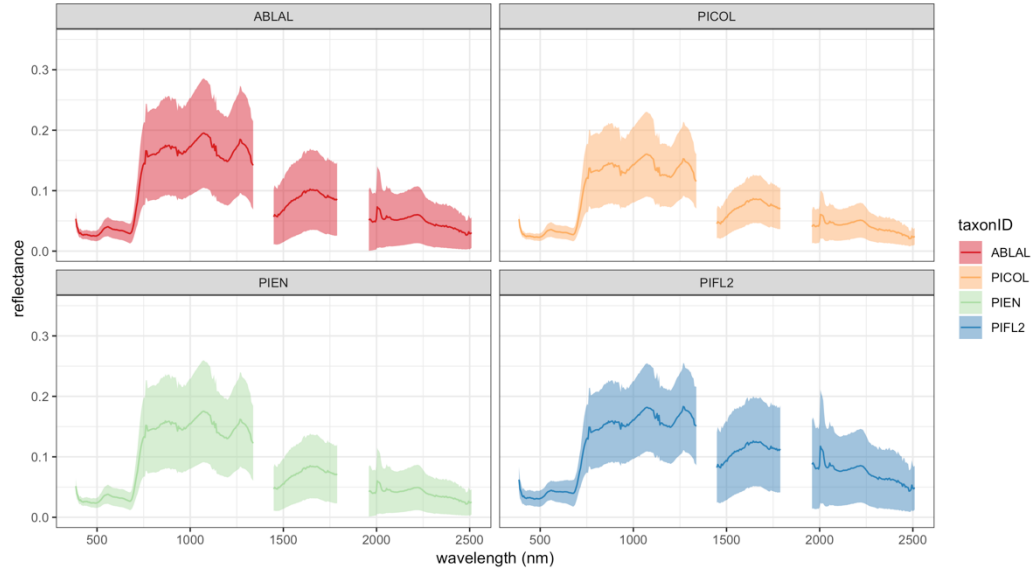


Figure A6: Mean spectral reflectance per species extracted from neon_veg max-diameter polygons.

Appendix B. Spectral reflectance curves overlaid

To compare the magnitudes and well-defined differences between species, the mean spectral reflectance curves \pm one standard deviation were overlaid.

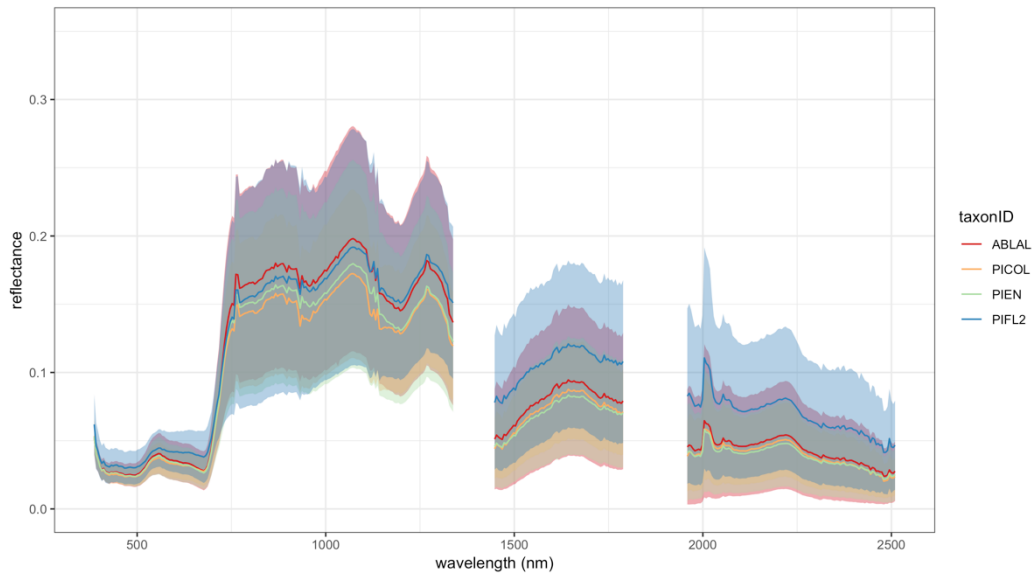


Figure B1. Mean spectral reflectance curves with shaded ± 1 standard deviation overlaid to compare reflectance magnitudes across all four species for all tree stem points.

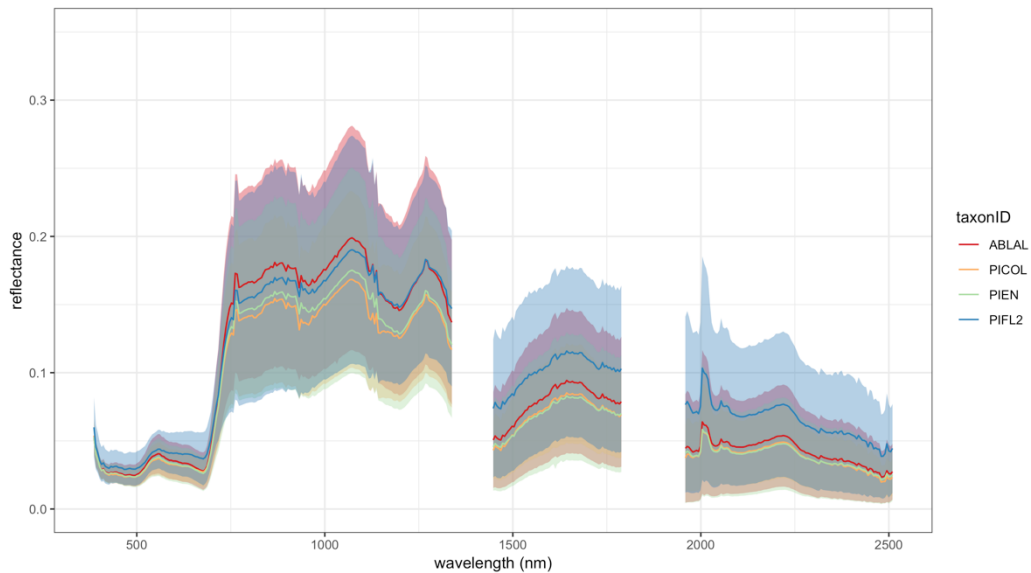


Figure B2. Mean spectral reflectance curves with shaded ± 1 standard deviation overlaid to compare reflectance magnitudes across all four species for all half-diameter polygons.

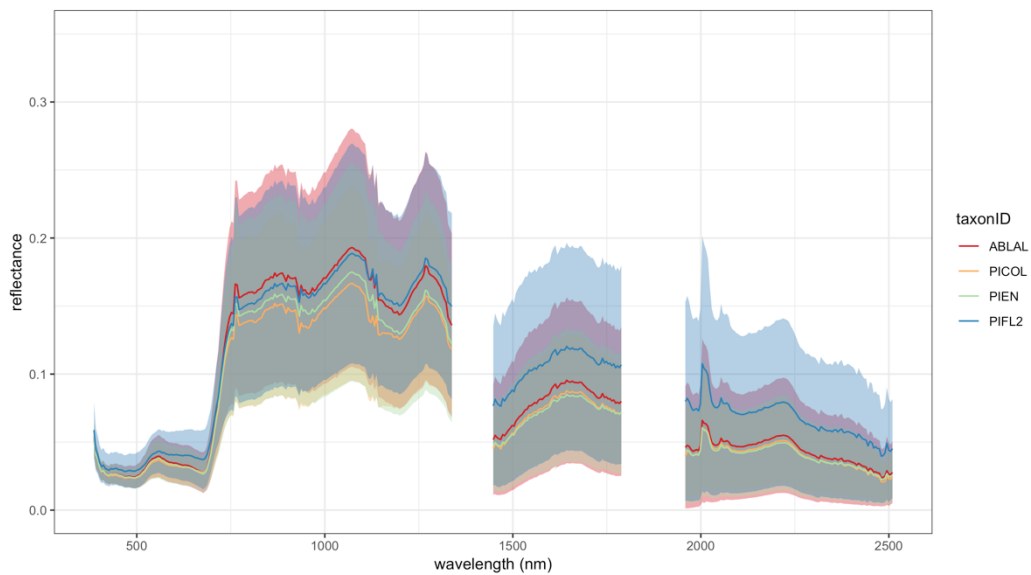


Figure B3. Mean spectral reflectance curves with shaded ± 1 standard deviation overlaid to compare reflectance magnitudes across all four species for all max-diameter polygons.

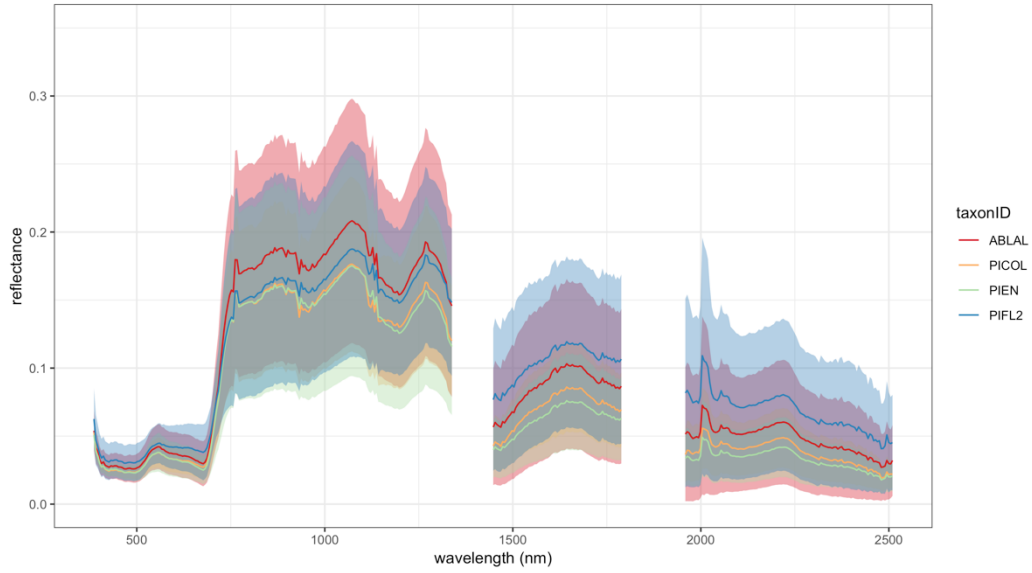


Figure B4. Mean spectral reflectance curves with shaded ± 1 standard deviation overlaid to compare reflectance magnitudes across all four species for neon_veg tree stem points.

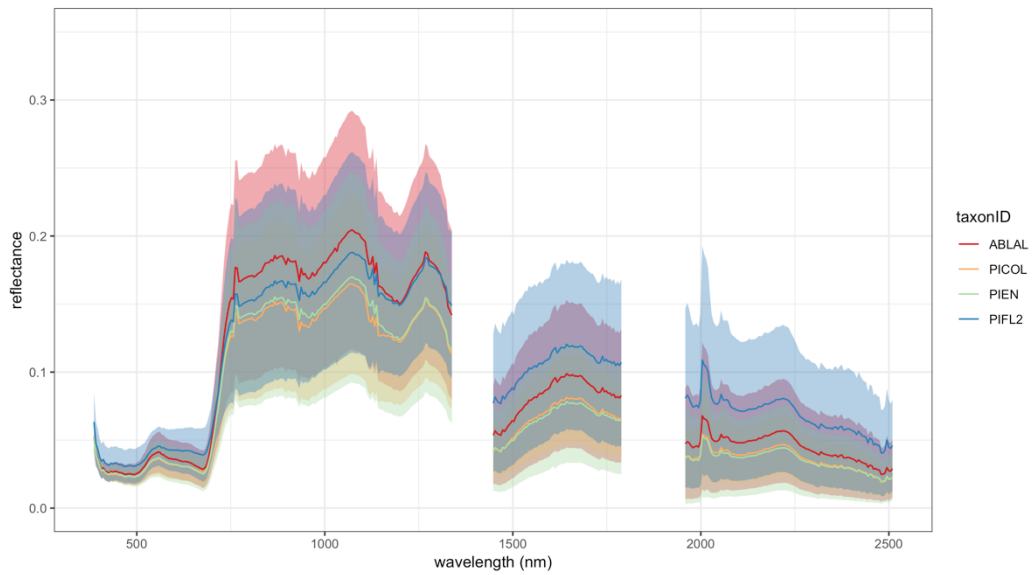


Figure B5. Mean spectral reflectance curves with shaded ± 1 standard deviation overlaid to compare reflectance magnitudes across all four species for neon_veg half-diameter polygons.

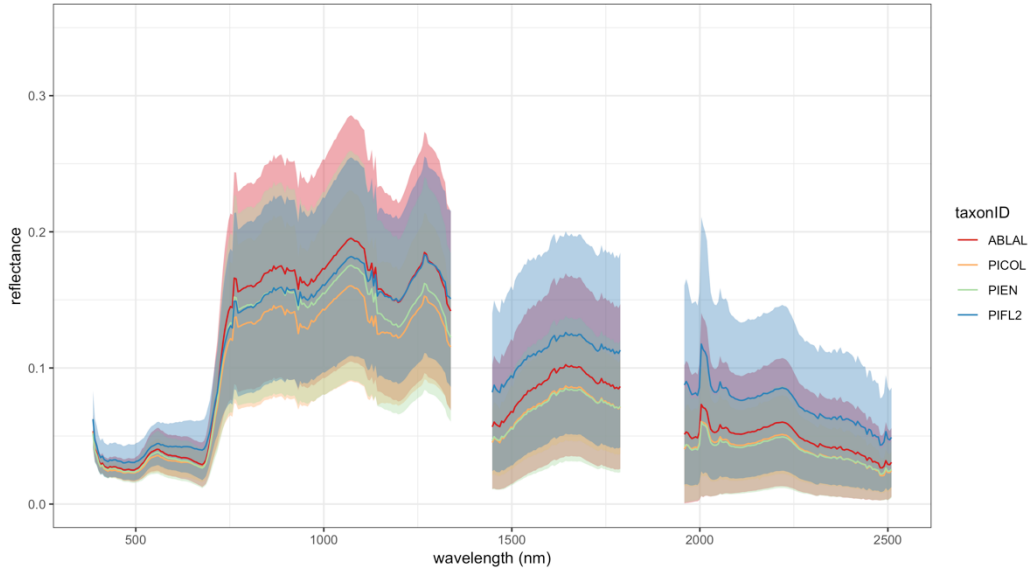


Figure B6. Mean spectral reflectance curves with shaded ± 1 standard deviation overlaid to compare reflectance magnitudes across all four species for neon_veg max-diameter polygons.

Appendix C. Interspecies comparison of variables

To compare the distribution of variables across the species, boxplots were created for the six most important variables (as ranked by MDA) for each of the reference sets.

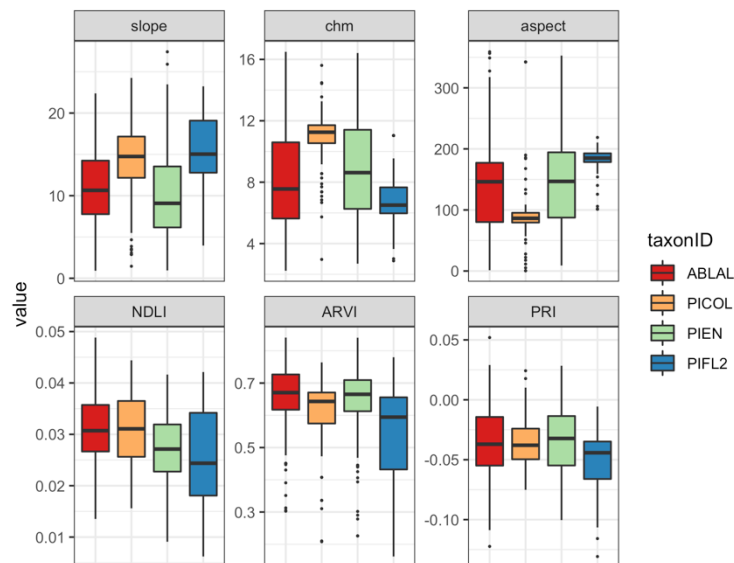


Figure C1. Interspecies comparison of most important remote sensing variables extracted by all tree stem points.

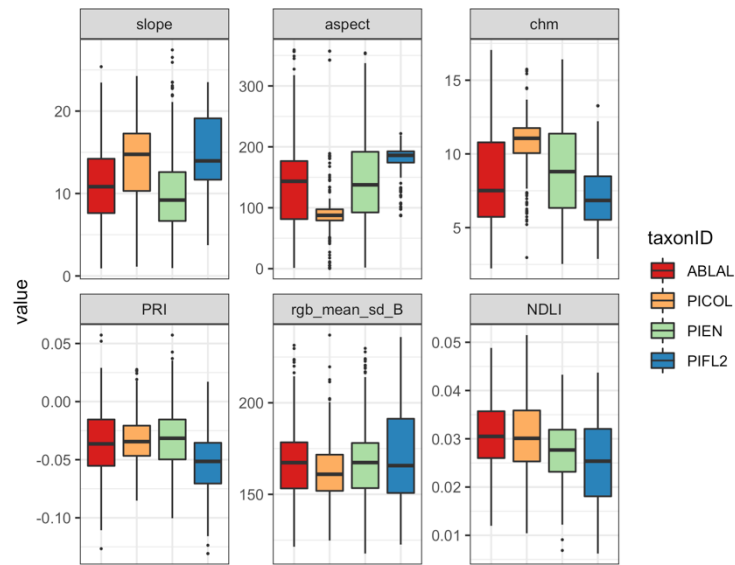


Figure C2. Interspecies comparison of most important remote sensing variables extracted by all half-diameter polygons.

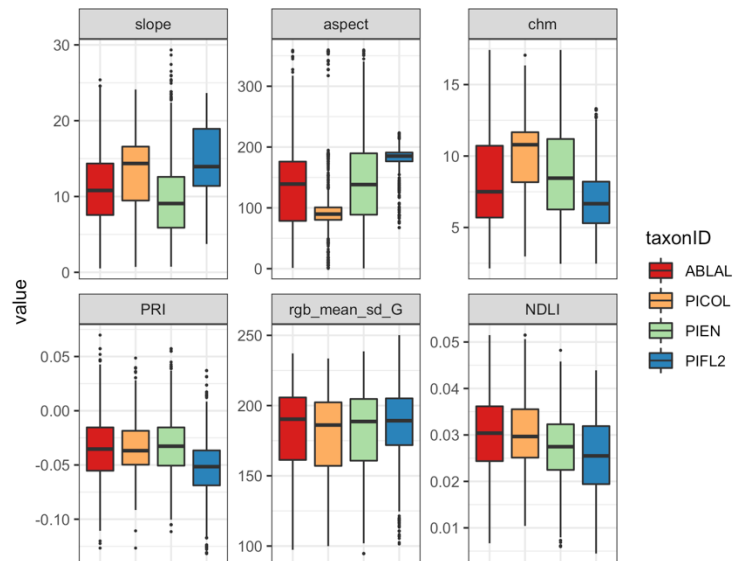


Figure C3. Interspecies comparison of most important remote sensing variables extracted by all max-diameter polygons.

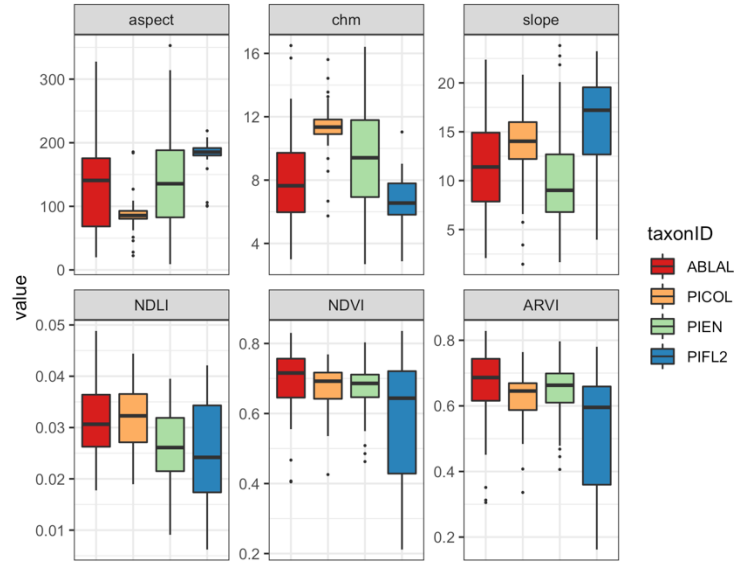


Figure C4. Interspecies comparison of most important remote sensing variables extracted by neon_veg tree stem points.

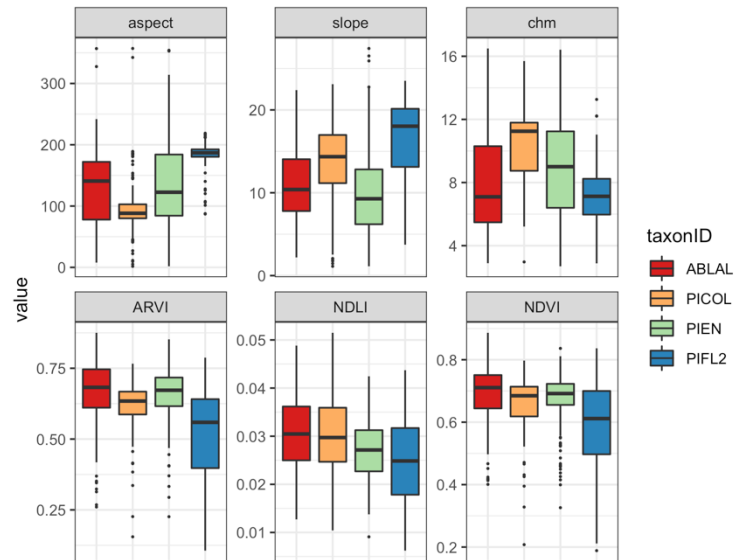


Figure C5. Interspecies comparison of most important remote sensing variables extracted by neon_veg half-diameter polygons.

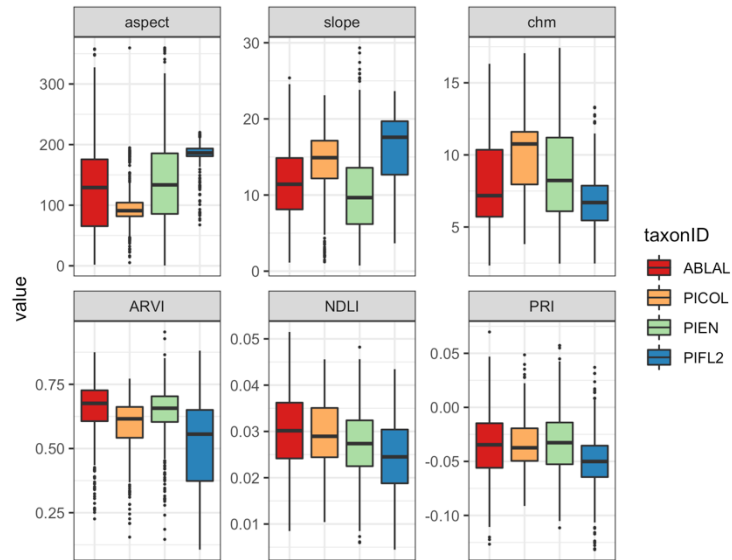


Figure C6. Interspecies comparison of most important remote sensing variables extracted by neon_veg max-diameter polygons.

Appendix D. Variable importance

Variable importance was quantified for each of the RF models based on the MDA metric and displayed as horizontal bar charts.

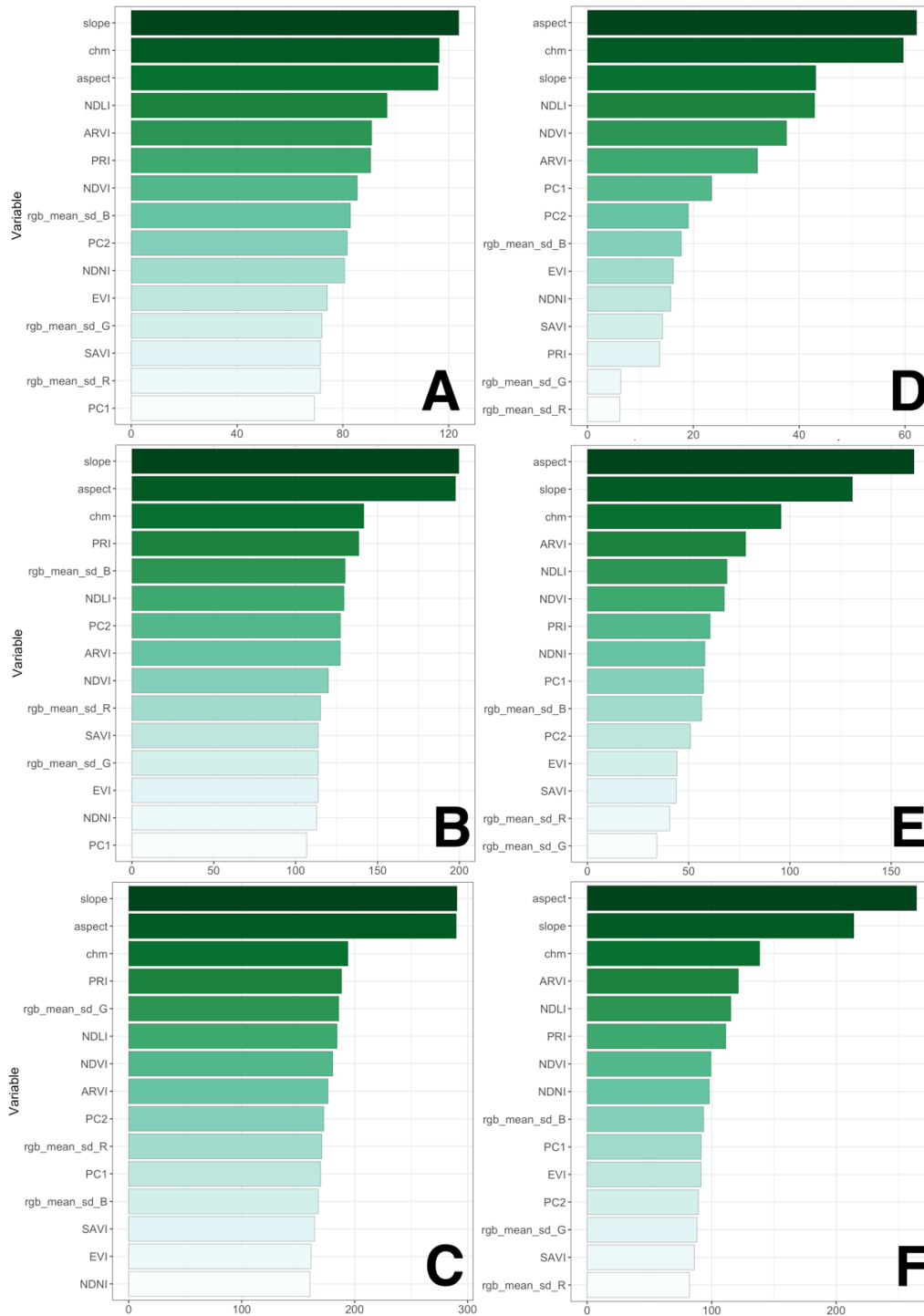


Figure D1: Variable importance ranked by MDA for (A) all stem points, (B) all half-diameter polygons, (C) all maximum-diameter polygons, (D) neon_veg stem points, (E) neon_veg half-diameter polygons, and (F) neon_veg polygons maximum-diameter polygons.